日本磁気学会
ISSN 2432-0250
Journal of the Magnetics Society of Japan
Electronic Journal URL: https://www.jstage.jst.go.jp/browse/msjmag

Vol.47 No.3 2023

Journal

JOURNAL OF THE MAGNETICS SOCIETY OF JAPAN

Vol.47 No.3 2023

日本磁気学会

ISSN 2432-0250

HP: http://www.magnetics.jp/ e-mail: msj@bj.wakwak.com

Electronic Journal: http://www.jstage.jst.go.jp/browse/msjmag

Journal of the Magnetics Society of Japan
Vol. 47, No. 3

Electronic Journal URL: https://www.jstage.jst.go.jp/browse/msjmag

CONTENTS

J. Magn. Soc. Jpn., **47**, 57-65 (2023) <Paper>

Information Degradation in Heated-Dot Magnetic Recording

T. Kobayashi and Y. Nakatani*

Graduate School of Engineering, Mie Univ., *1577 Kurimamachiya-cho, Tsu 514-8507, Japan*

*Graduate School of Informatics and Engineering, Univ. of Electro-Communications, *1-5-1 Chofugaoka, Chofu 182-8585, Japan*

In this work, we focus on three factors as regards information degradation in 4 Tbpsi heated-dot magnetic recording, namely, (1) the reduction in readout field strength due to dot area variation, (2) the reversal of the magnetization direction during 10 years of archiving due to thermal fluctuation, and (3) during adjacent track writing due to thermal fluctuation (adjacent track interference, ATI). We consider the full width at half maximum of the readout field as well as the peak value. The bit error rate bER as a function of the minimum normalized readout field H_0, that must be readable without error, is calculated using each dot error probability, taking account of dot area variation and thermal fluctuation. The H_0 value needed to achieve a certain bER is determined by dot area variation. There is a minimum dot height for a certain bER, which is determined by thermal fluctuation. Even if the dot height is increased, the H_0 value cannot be increased. Since temperature has a strong impact on dot error probability, a very large thermal gradient in the cross-track direction is needed to suppress ATI.

Key words: HDMR, dot area variation, thermal fluctuation, readout field, 10 years of archiving, adjacent track interference

1. Introduction

Many magnetic recording methods have been proposed to solve the trilemma problem[1] of conventional magnetic recording (CMR) on granular media, for example, shingled magnetic recording (SMR), microwave-assisted magnetic recording (MAMR), heat-assisted magnetic recording (HAMR), bit patterned media (BPM), and three-dimensional magnetic recording (3D MR).

Akagi *et al.* reported the recording performance of heated-dot magnetic recording (HDMR), namely HAMR on BPM[2]. Yamane *et al.* reported the recording performance of 3D HDMR[3]. We have previously discussed information stability during 10 years of archiving[4] and during adjacent track writing[5] for HAMR on granular media. And we have also compared 4 Tbpsi HAMR and 2 Tbpsi/layer 3D HAMR on granular media in terms of information stability during 10 years of archiving, during adjacent track writing, and writing sensitivity[6].

In this paper, we discuss information degradation due to dot area variation and thermal fluctuation in 4 Tbpsi HDMR. There are three factors as regards information degradation:

(1) Reduction in readout field strength due to dot area variation,

(2) Reversal of magnetization direction during 10 years of archiving due to thermal fluctuation, and

(3) Reversal of magnetization direction during adjacent track writing due to thermal fluctuation (adjacent track interference, ATI).

We examine the above three factors below.

2. Calculation Condition and Method

2.1 Dot arrangement and medium structure

Figure 1 shows the dot arrangement and medium structure in 4 Tbpsi HDMR where D_x, D_y, and h are the dot sizes for the down-track and cross-track directions, and the dot height, respectively. We assumed that the mean dot size D_m and dot spacing Δ_D are the same for both the down-track and cross-track directions, namely $D_\mathrm{m} = \Delta_\mathrm{D} = 6.4$ nm. The bit length D_B and track width D_T were 12.7 nm. The writing temperature T_w for the dot was assumed to be $T_\mathrm{cm} + 3\sigma_\mathrm{Tc}$ where T_cm and σ_Tc are the mean Curie temperature and standard deviation of T_cm, respectively, taking account of the Curie temperature T_c variation. The T_c distribution was assumed to be normal. While writing, the probability is 99.9 % where the T_c value of the dot is lower than T_w, namely $T_\mathrm{c} < T_\mathrm{w}$.

We considered that there are dependent and independent cases for the dot sizes D_x and D_y according to the dot manufacturing method as shown in Fig. 2. The dependent and independent cases mean (a) square $D_x = D_y$ dot and (b) rectangular $D_x \neq D_y$ dot, respectively. We examined both cases.

We generated random number D_x according to a log-normal distribution with a standard deviation σ_D. The σ_D values were assumed to be equal in the down-track and cross-track directions. For $D_x = D_y$ case, we used D_x as D_y. On the other hand, we generated random number D_y independently for $D_x \neq D_y$ case. The variation of the dot area D_xD_y was smaller for $D_x \neq D_y$ case, since the dot sizes D_x and D_y were determined independently.

Corresponding author: T. Kobayashi (e-mail: kobayasi @phen.mie-u.ac.jp).

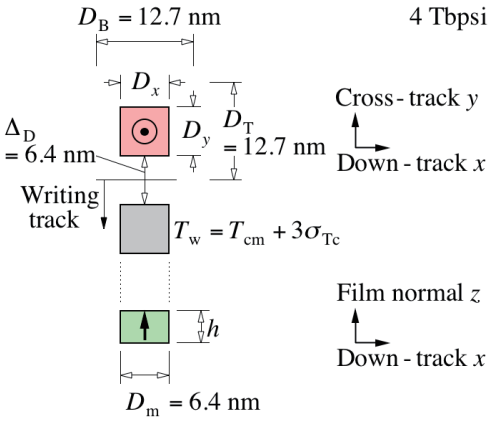

Fig. 1 Dot arrangement and medium structure.

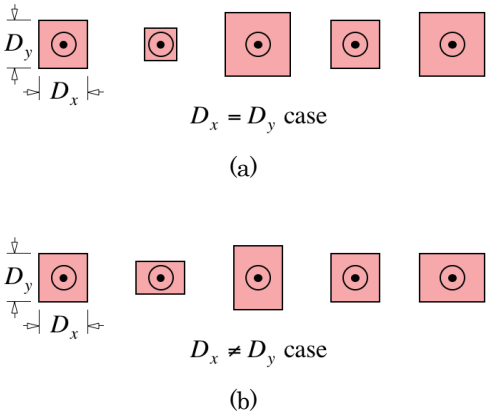

Fig. 2 (a) Dependent $D_x = D_y$ and (b) independent $D_x \neq D_y$ cases for dot sizes D_x and D_y.

2.2 Field strength

The readout field strength was calculated at the magnetic head reader, which was located 4.0 nm above the magnetic layer surface.

We assumed that the magnetization $M_s(T_{cm}, 330\ \mathrm{K})$ was 958 emu/cm^3 at a readout temperature of 330 K. Figure 3 (a) shows the z component $H_z(D_x, D_y, h)$ of the readout field against the cross-track direction for $D_x = D_y$ values of 6.4 and 4.4 nm and an h value of 4 nm where H_{zpeak} is the peak $H_z(D_x, D_y, h)$ value. When the $D_x = D_y$ value is small, the full width at half maximum FWHM in $H_z(D_x, D_y, h)$ is also small as well as the H_{zpeak} value. We considered the FWHM^2 value, taking account of the FWHM values for the cross-track and down-track directions. The $\mathrm{FWHM}^2 \times H_{zpeak}$ value is almost proportional to the dot area D_xD_y as shown in Fig. 3 (b). Therefore, the readout field is approximated as being proportional to the surface magnetic charge $M_s(T_c, 330\ \mathrm{K})D_xD_y$ of the dot, taking account of the T_c variation.

2.3 Magnetic properties

The temperature dependence of the medium magnetization M_s was calculated by employing mean field analysis[7], and that of the medium anisotropy

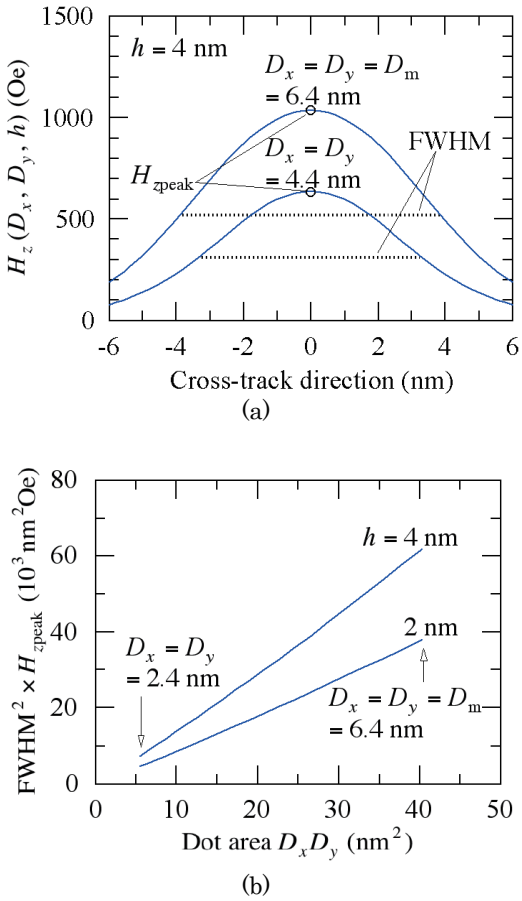

Fig. 3 (a) z component $H_z(D_x, D_y, h)$ of readout field against cross-track direction and (b) $\mathrm{FWHM}^2 \times H_{zpeak}$ value as a function of dot area D_xD_y.

constant K_u was assumed to be proportional to M_s^2[8]. $M_s(T_c, T)$ is a function of the Curie temperature T_c and temperature T. $M_s(T_c = 770\ \mathrm{K}, T = 300\ \mathrm{K})$ = 1000 emu /cm^3 was assumed for FePt. Based on this assumption, the M_s value can be calculated for all values of T_c and T.

We have introduced an HAMR medium parameter, namely, the medium anisotropy constant ratio K_u/K_{bulk}[9] in place of K_u. K_u/K_{bulk} is the intrinsic ratio of the medium K_u to bulk FePt K_u, which is independent of T_c, and is valid for any temperature from zero Kelvin to the Curie temperature. The $K_u(T_c, K_u/K_{bulk}, T)$ value is a function of T_c, K_u/K_{bulk}, and T. $K_u(T_c = 770\ \mathrm{K}, K_u/K_{bulk} = 1, T = 300\ \mathrm{K})$ = 70 Merg/cm^3 was assumed for bulk FePt. Using this assumption, we can calculate the K_u value for all values of T_c, K_u/K_{bulk}, and T. No intrinsic distribution of K_u was assumed. However, there was a fluctuation in K_u caused by T_c variation.

The T_c value can be adjusted by changing the Cu composition z for $(Fe_{0.5}Pt_{0.5})_{1-z}Cu_z$.

We used a T_{cm} value of 750 K with a σ_{Tc}/T_{cm} value of 2 % and a K_u/K_{bulk} value of 0.8, thus giving a K_u value of 51 Merg/cm^3 and an anisotropy field H_k of 107 kOe at the readout temperature of 330 K in this paper.

2.4 Temperature profile

Since the thermal gradient during the writing period can be adjusted by changing the medium structure, we used the thermal gradients $\partial T/\partial y$ of 10 to 18 K/nm in the cross-track direction when we examined adjacent track interference. For simplicity, $\partial T/\partial y$ was assumed to be constant anywhere, and $\partial T/\partial x$ in the down-track direction was zero, since $\partial T/\partial x$ does not affect the results.

2.5 Information stability

The bit error rate bER was calculated by employing each dot error probability P,

$$P = 1 - \exp\left(-f_0 t \exp\left(-\frac{K_{\mathrm{ueff}}V}{kT}\left(1+\frac{H_{\mathrm{w}}}{H_{\mathrm{keff}}}\right)^2\right)\right), \quad (1)$$
$$(|H_{\mathrm{w}}| < H_{\mathrm{keff}})$$

taking account of the shape anisotropy $M_{\mathrm{s}}H_{\mathrm{d}}/2$ using a self-demagnetizing field H_{d} where f_0, t, $K_{\mathrm{ueff}} = K_{\mathrm{u}} - M_{\mathrm{s}}H_{\mathrm{d}}/2$, $V = D_x D_y \times h$, k, T, H_{w}, and $H_{\mathrm{keff}} = 2K_{\mathrm{ueff}}/M_{\mathrm{s}}$ are, respectively, the attempt frequency[10], time, effective anisotropy constant, dot volume, Boltzmann constant, dot temperature, writing field, and effective anisotropy field. The demagnetizing field inside the dot was included, but the magnetostatic field from surrounding dots was neglected. The f_0 value is a function of the Gilbert damping constant α[10]. The α value used here was 0.1 without temperature dependence, since the α value and its temperature dependence for FePt are not currently known.

We introduced a minimum normalized readout field H_0 after information degradation, which is the minimum readout field for signal processing and is normalized by that from the dot with T_{cm} and D_{m}, since the bER value is determined by the signal processing as well as medium properties. A H_0 of 1.0 corresponds to the readout field from the dot with T_{cm} and D_{m}. When H_0 is zero, the readout field is also zero. If the signal processing cannot extract the correct information from the readout signal, the bER value will increase. If the signal processing requires a large signal amplitude, the bER value will be high, and if a small signal amplitude is acceptable, the bER value will be low. The bER value is a function of H_0. The criterion determining whether or not information is stable was assumed to be a bER of 10^{-3}. Therefore, the signal processing is required to read a certain H_0 value without error for a bER of 10^{-3}. The calculation bit number was 10^7.

The bit error rate bER_0, where the magnetization direction is parallel to the recording direction, is expressed as

$$\mathrm{bER}_0 = Er(1-P). \quad (2)$$

The bit error rate bER_1, where the magnetization direction is antiparallel to the recording direction, is expressed as

$$\mathrm{bER}_1 = P. \quad (3)$$

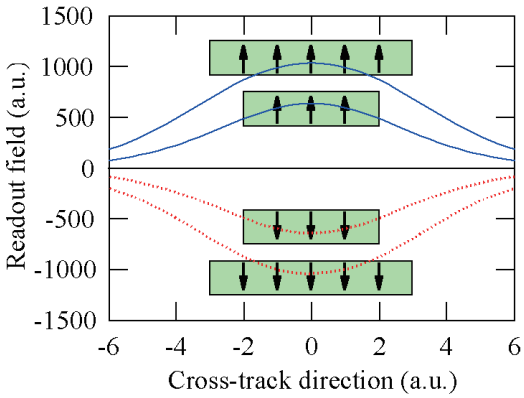

Fig. 4 Schematic illustration of readout field degradation caused by reduction in readout field strength shown by solid lines and reversal of magnetization direction shown by dotted lines.

Table 1 Calculation conditions.

Recording density (Tbpsi)	4
Mean dot size D_{m} (nm)	6.4
Standard deviation $\sigma_{\mathrm{D}}/D_{\mathrm{m}}$ (%) of D_{m}	variable
Dot sizes D_x and D_y (nm)	log-normal distr.
Dot height h (nm)	variable
Dot spacing Δ_{D} (nm)	6.4
Bit length D_{B} (nm)	12.7
Track width D_{T} (nm)	12.7
Mean Curie temperature T_{cm} (K)	750
Standard deviation $\sigma_{\mathrm{Tc}}/T_{\mathrm{cm}}$ (%) of T_{cm}	2
Curie temperature T_{c} (K)	normal distr.
Anisotropy constant ratio $K_{\mathrm{u}}/K_{\mathrm{bulk}}$	0.8
Gilbert damping constant α	0.1

In Eq. (2),

$$Er = 1, \text{ if } \frac{M_{\mathrm{s}}(T_{\mathrm{c}},330\ \mathrm{K})D_xD_y}{M_{\mathrm{s}}(T_{\mathrm{cm}},330\ \mathrm{K})D_{\mathrm{m}}^2} \le H_0, \quad (4)$$

and

$$Er = 0, \text{ if } \frac{M_{\mathrm{s}}(T_{\mathrm{c}},330\ \mathrm{K})D_xD_y}{M_{\mathrm{s}}(T_{\mathrm{cm}},330\ \mathrm{K})D_{\mathrm{m}}^2} > H_0. \quad (5)$$

Figure 4 shows a schematic illustration of the readout field degradation. The bit error rates bER_0 and bER_1 are caused by the reduction in readout field strength shown by solid lines in Fig. 4 and the reversal of magnetization direction shown by dotted lines, respectively. In Eqs. (4) and (5), the numerator $M_{\mathrm{s}}(T_{\mathrm{c}},330\ \mathrm{K})D_xD_y$ is the surface magnetic charge of a dot that is magnetized in the recording direction, and denominator $M_{\mathrm{s}}(T_{\mathrm{cm}},330\ \mathrm{K})D_{\mathrm{m}}^2$ is the surface magnetic charge of the dot with T_{cm} and D_{m}. Using the approximation shown above in Fig. 3 (b), if the ratio of $M_{\mathrm{s}}(T_{\mathrm{c}},330\ \mathrm{K})D_xD_y$ to $M_{\mathrm{s}}(T_{\mathrm{cm}},330\ \mathrm{K})D_{\mathrm{m}}^2$ of each dot is smaller than H_0 as shown in Eq. (4), the dot was assumed to be error. The total bER is the summation of two bER values as follows

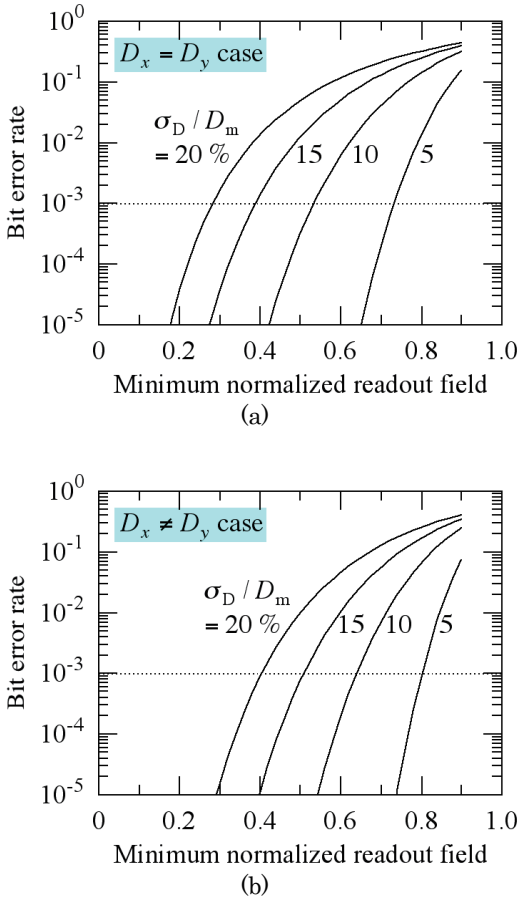

Fig. 5 Bit error rate bER as a function of minimum normalized readout field H_0 for various σ_D/D_m values in (a) $D_x = D_y$ and (b) $D_x \neq D_y$ cases.

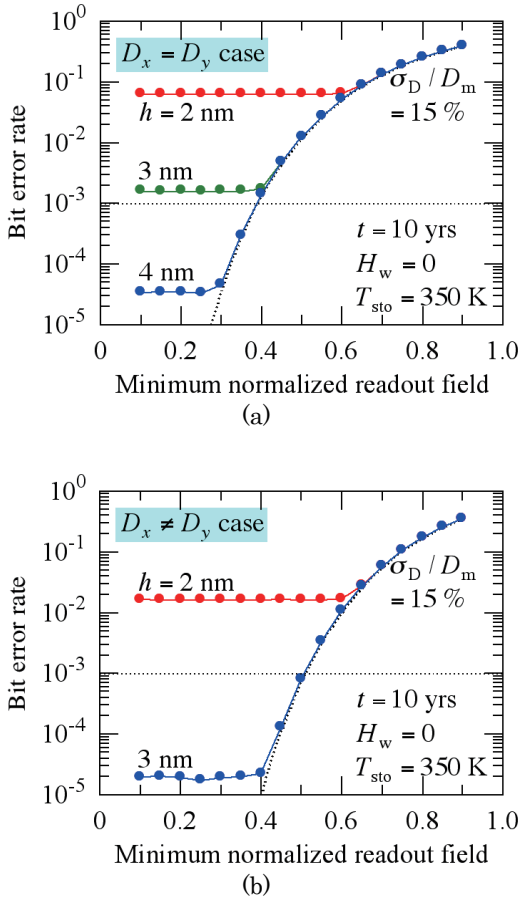

Fig. 6 Bit error rate bER as a function of minimum normalized readout field H_0 after 10 years for various h values in (a) $D_x = D_y$ and (b) $D_x \neq D_y$ cases.

$$\mathrm{bER} = \mathrm{bER}_0 + \mathrm{bER}_1. \quad (6)$$

The calculation conditions are summarized in Table 1.

The bER and H_0 values for "010" data in this paper are useful only for comparisons.

3. Calculation Results

3.1 Reduction in readout field strength due to dot area variation

We first examined of the reduction in the readout field strength due to dot area variation.

Even if the effective thermal stability factor $K_{ueff}V/(kT) = K_{ueff}(D_xD_y \times h)/(kT)$ is sufficiently large, namely $P = 0$, a dot with a size

$$D_x < D_m\sqrt{H_0} \quad (7)$$

will be error due to dot area variation for $D_x = D_y$. The bER value is equal to the cumulative distribution function. Figure 5 (a) shows the bER value as a function of H_0 for various σ_D/D_m values when $D_x = D_y$. When σ_D/D_m = 20 %, signal processing is needed to read a small H_0 value of 0.28 without error for a bER of 10^{-3}. On the other hand, it is only necessary to read a large H_0 value of 0.73, when σ_D/D_m = 5 %.

Similarly, the result is shown in Fig. 5 (b) for $D_x \neq D_y$. Even with the same σ_D/D_m, the variation in the dot area becomes smaller for $D_x \neq D_y$. Therefore, an H_0 value of 0.41 is sufficient for the signal processing even if σ_D/D_m = 20 %.

3.2 Reversal of magnetization direction during 10 years of archiving due to thermal fluctuation

Next, we discuss the reversal of the magnetization direction during 10 years of archiving due to thermal fluctuation.

The H_w value was zero and the storage temperature T_{sto} was 350 K. We took a certain margin for temperature into account.

Figure 6 (a) shows the bER value as a function of H_0 after 10 years of archiving for various dot heights h in $D_x = D_y$ case when σ_D/D_m = 15 %. The dotted line shows the result in Fig. 5 (a). When the H_0 value is large, the limiting factor for bER is dot area variation determined by σ_D/D_m, which is the same with that shown in Fig. 5 (a). Otherwise, the limiting factor is thermal fluctuation determined by $K_{ueff}V/(kT)$. Since one bit consists of one dot, the bER value is independent of the H_0 value at the range where the thermal fluctuation is dominant. The bER value decreases as the h value increases. However, even if the h value is

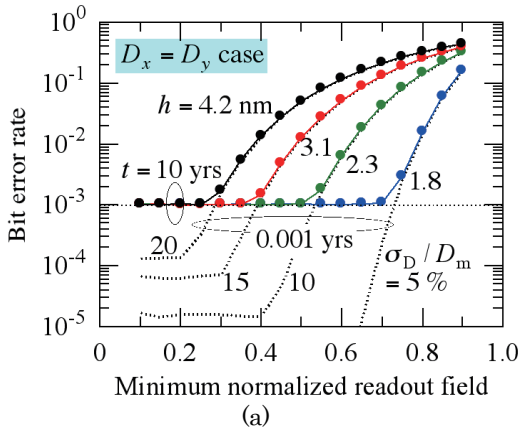

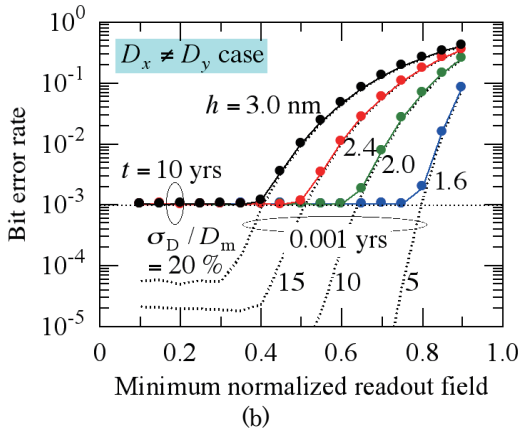

Fig. 7 Bit error rate bER as a function of minimum normalized readout field H_0 after 10 and 0.001 years for various σ_D/D_m values in (a) $D_x = D_y$ and (b) $D_x \neq D_y$ cases.

increased, the H_0 value cannot be increased. As shown in Fig. 6 (b), the bER value in $D_x \neq D_y$ case is smaller than that shown in Fig. 6 (a) for the same h value, since the variation of the dot area becomes smaller.

As seen in Fig. 7 (a), the h values needed to achieve a bER of 10^{-3} after 10 years of archiving are 1.8 to 4.2 nm for σ_D/D_m values of 5 to 20 %, respectively, when $D_x = D_y$. Some information degradation from 0.001 to 10 years can be seen where 0.001 years corresponds about 9 hours. If the information degradation is of concern, we can choose a larger dot height so that the bER decreases to less than 10^{-4} after 10 years as shown in Fig. 6 (a). The result for $D_x \neq D_y$ is shown in Fig. 7 (b).

We defined the information degradation rate R_0 during 10 years of archiving as

$$R_0 = \frac{\mathrm{bER(10\ yrs)} - \mathrm{bER(0.001\ yrs)}}{\mathrm{bER(0.001\ yrs)}}. \quad (8)$$

The R_0 value for no information degradation is less than about 0.1, since the R_0 value is 0.11 when $\mathrm{bER(10\ yrs)} = 10^{-3}$ and $\mathrm{bER(0.001\ yrs)} = 9\times10^{-4}$.

The H_0, h, and $K_{ueff}V/(kT)$ conditions needed to achieve a bER of 10^{-3}, and R_0 for various σ_D/D_m values are summarized in Table 2. As the σ_D/D_m value

Table 2 Minimum normalized readout field H_0, dot height h, and effective thermal stability factor $K_{ueff}V/(kT)$ to achieve a bER of 10^{-3}, and information degradation rate R_0 for various σ_D/D_m values for (a) $D_x = D_y$ and (b) $D_x \neq D_y$ cases.

(a)

σ_D / D_m (%) ($D_x = D_y$ case)	H_0	h (nm)	$\frac{K_{ueff}V}{kT}$ (350 K)	R_0
5	0.73	1.8	67	1477
10	0.53	2.3	90	63
15	0.39	3.1	121	14
20	0.28	4.2	165	6.5

(b)

σ_D / D_m (%) ($D_x \neq D_y$ case)	H_0	h (nm)	$\frac{K_{ueff}V}{kT}$ (350 K)	R_0
5	0.80	1.6	63	3835
10	0.64	2.0	76	265
15	0.51	2.4	94	49
20	0.41	3.0	117	17

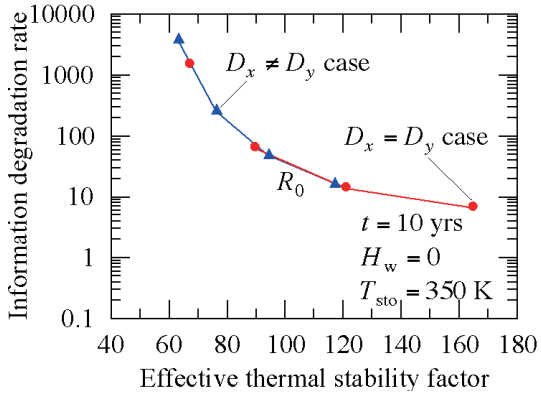

Fig. 8 Information degradation rate R_0 as a function of effective thermal stability factor $K_{ueff}V/(kT)$ for $D_x = D_y$ and $D_x \neq D_y$ cases.

increases, the H_0 value decreases due to dot area variation and the h value increases due to thermal fluctuation. However, the h value is relatively small; thus 10 years of archiving is easy to realize. If the σ_D/D_m values are the same, the $K_{ueff}V/(kT)$ value to achieve a bER of 10^{-3} for $D_x = D_y$ is larger than that for $D_x \neq D_y$ because of the larger dot area variation. The R_0 value decreases as the $K_{ueff}V/(kT)$ value increases as shown in Table 2 and Fig. 8. Figure 8 shows that regardless of $D_x = D_y$ and $D_x \neq D_y$, if the $K_{ueff}V/(kT)$ values are the same, the R_0 values are the same.

We roughly evaluated the readout property using the product of $\mathrm{FWHM}^2 \times H_{zpeak} \times H_0$ where FWHM^2 and H_{zpeak} are values for D_m. The FWHM^2 and H_{zpeak} values, and the $\mathrm{FWHM}^2 \times H_{zpeak} \times H_0$ product for a bER of 10^{-3} are summarized in Table 3. The FWHM^2 and

Table 3 FWHM^2 in z component H_z of readout field, peak z component H_{zpeak}, and FWHM$^2 \times H_{zpeak} \times H_0$ product for various σ_D/D_m values in (a) $D_x = D_y$ and (b) $D_x \neq D_y$ cases.

(a)

σ_D / D_m (%) ($D_x = D_y$ case)	FWHM^2 (nm^2)	H_{zpeak} (Oe)	FWHM$^2 \times H_{zpeak} \times H_0$ (10^3 nm^{2}Oe)
5	53	649	25
10	55	778	23
15	57	918	20
20	60	1056	18

(b)

σ_D / D_m (%) ($D_x \neq D_y$ case)	FWHM^2 (nm^2)	H_{zpeak} (Oe)	FWHM$^2 \times H_{zpeak} \times H_0$ (10^3 nm^{2}Oe)
5	53	617	26
10	54	701	24
15	55	799	23
20	57	900	21

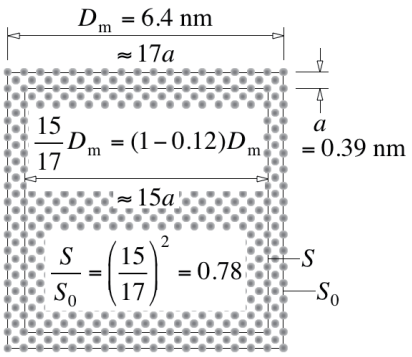

Fig. 9 Schematic illustration of dot.

H_{zpeak} values increase as the σ_D/D_m value increases, since the h value increases as shown in Table 2. However, the FWHM$^2 \times H_{zpeak} \times H_0$ product decreases, since the H_0 value decreases as shown in Table 2.

The H_0 value in the FWHM$^2 \times H_{zpeak} \times H_0$ product is determined by the σ_D/D_m value as shown in Fig. 5. Even if the h value is increased, the H_0 value cannot be increased as shown in Fig. 6. Figure 9 is a schematic illustration of the top view of a dot using Fe or Pt atoms. Since the D_m value is 6.4 nm and the lattice constant a of FePt is 0.39 nm, one side of the dot consists of about 17 lattice constants. A dot, whose top, bottom, left, and right are one lattice constant smaller, is about 12 % shorter in length. Since the dot area decreases to about 78 %, the FWHM$^2 \times H_{zpeak}$ value will decrease to 78 % as shown in Fig. 3 (b). Therefore, to reduce the σ_D/D_m value, it is necessary to manufacture dots with an accuracy of the order of the lattice constant.

To increase the H_{zpeak} value in the FWHM$^2 \times H_{zpeak} \times H_0$ product, it is necessary to increase the dot height h as shown in Fig. 10.

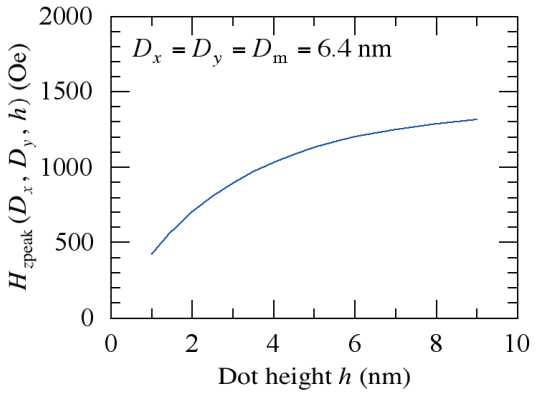

Fig. 10 H_{zpeak} value of readout field as a function of dot height h.

We have previously reported the R_0 value for 4 Tbpsi shingled HAMR with a σ_D/D_m value of 15 %[6], in which the R_0 value was less than 0.1, and no information degradation can be seen during 10 years. Therefore, we compared the H_0 dependence of the bER for BPM and granular media. Figure 11 shows the H_0 dependence of the bER after 10 and 0.001 years for various σ_D/D_m values in 4 Tbpsi shingled HAMR under the conditions reported in a previous paper[6]. Although one bit has 6 grains, the bER value was calculated using 4 grains, since 2 grains were used as a guard band for ATI. In comparison with the results in Fig. 7, the bER value decreases as the H_0 value decreases. The R_0 values are less than 0.1, namely no information degradation, for σ_D/D_m = 5, 10, and 15 %. Referring to Fig. 8, the R_0 value for granular media is much smaller than that for BPM, since the $K_{ueff}V/(kT)$ value at 350 K is 152 for granular media.

This difference in the H_0 dependence of the bER can be explained using Fig. 12, which shows the H_0 dependence of the bER for various dot or grain error probabilities P in (a) BPM and (b) 4 grain granular media where all dots or grains are assumed to be homogeneous, namely σ_D/D_m = 0. For (b) granular media, the bER value is calculated for n grain errors out of m grains as

$$\text{bER} = \sum_n^m \binom{m}{n} (1-P)^{m-n} P^n, \quad (9)$$

and the H_0 value is represented by

$$H_0 = \frac{m-2n}{m}. \quad (10)$$

For (a) BPM, since one bit consists of one dot, the bER value is independent of the H_0 value. The dot error probability P must be as small as 0.001 for a bER of 10^{-3}. On the other hand, since one bit consists of several grains in (b) granular media, the bER value decreases as the H_0 value decreases for a statistical reason. A relatively high P value of more than 0.001 is allowed for a bER of 10^{-3} if a small H_0 is readable without error.

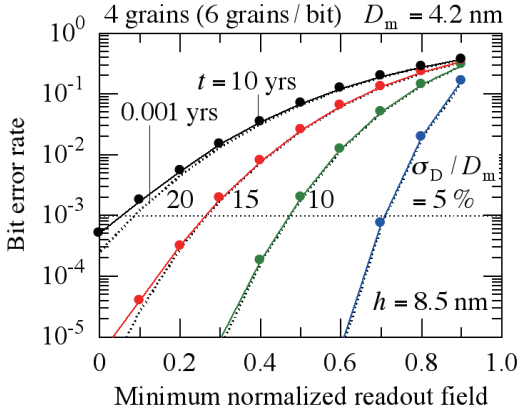

Fig. 11 Bit error rate bER as a function of minimum normalized readout field H_0 after 10 and 0.001 years for various σ_D/D_m values in 4 Tbpsi granular media.

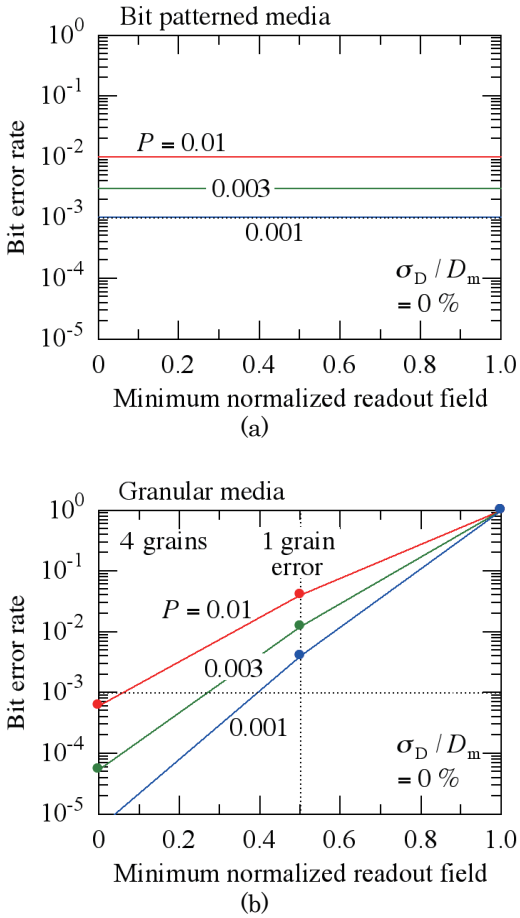

Fig. 12 Bit error rate bER as a function of minimum normalized readout field H_0 for various P values in (a) bit patterned media and (b) 4 grain granular media.

In addition to the results above, it is necessary to manufacture dots with a high accuracy such as of the order of the lattice constant in BPM, and to manufacture grains with a large grain aspect ratio h/D_m such as 2.0 in granular media[6].

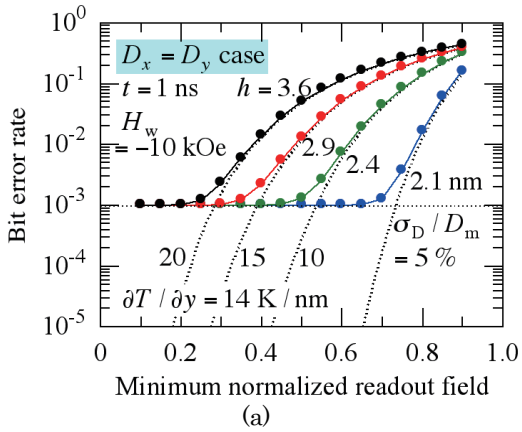

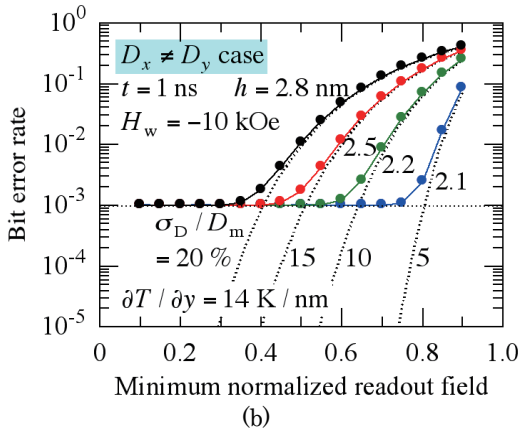

Fig. 13 Bit error rate bER as a function of minimum normalized readout field H_0 after adjacent track (AT) writing for various σ_D/D_m values in (a) $D_x = D_y$ and (b) $D_x \neq D_y$ cases (shingled HDMR).

3.3 Reversal of magnetization direction during adjacent track writing due to thermal fluctuation

Finally, we discuss the reversal of the magnetization direction during adjacent track (AT) writing due to thermal fluctuation, namely adjacent track interference (ATI). Since information stability in an adjacent track is necessary after a few and a 10^6 times rewrite for shingled and conventional HDMR, we used times of 1 ns and 1 ms, respectively. The H_w value was −10 kOe, namely 10 kOe antiparallel to the recording direction.

The standard deviation σ_{Tc} of T_c is equivalent to the standard deviation σ_y of the dot position for the cross-track direction as $\sigma_y = \sigma_{Tc}/(\partial T/\partial y)$. For example, σ_y is about 1 nm when the σ_{Tc}/T_{cm} and $\partial T/\partial y$ values are 2 % and 14 K/nm, respectively. Therefore, the value of 2 % includes σ_{Tc}/T_{cm} and σ_y/D_m.

Figure 13 shows the bER value as a function of H_0 after AT writing for various σ_D/D_m values in shingled HDMR where $\partial T/\partial y$ is 14 K/nm. Thus, the dot temperature adjacent to the writing dot is 617 K. The h values were adjusted so that the bER became 10^{-3} in the range where the thermal fluctuation is dominant. If a $\partial T/\partial y$ value of 14 K/nm can be achieved, the h values necessary for 10 years of archiving and ATI are roughly

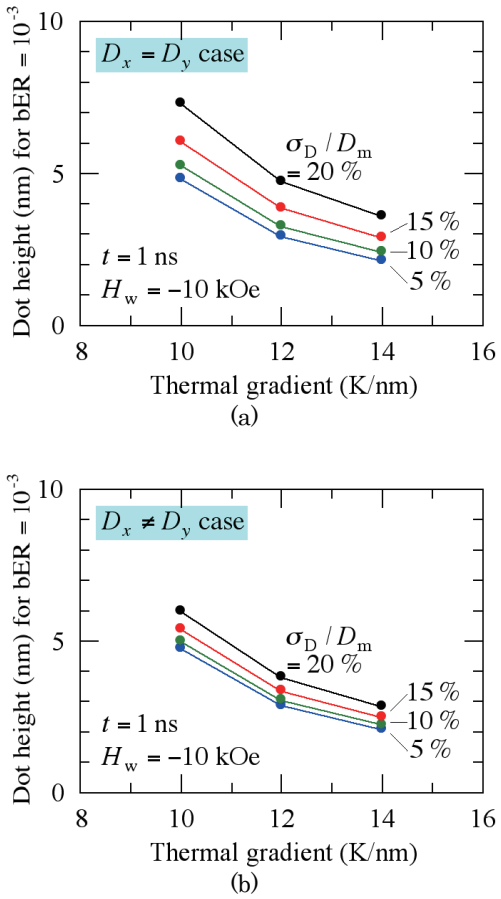

Fig. 14 Dot height h to achieve a bER of 10^{-3} as a function of thermal gradient $\partial T/\partial y$ after AT writing for various σ_D/D_m values in (a) $D_x = D_y$ and (b) $D_x \neq D_y$ cases (shingled HDMR).

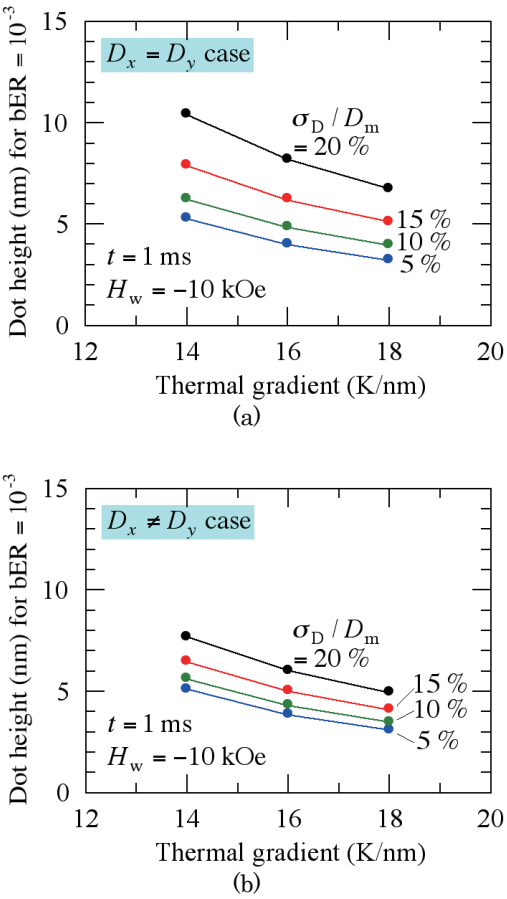

Fig. 15 Dot height h to achieve a bER of 10^{-3} as a function of thermal gradient $\partial T/\partial y$ after AT writing for various σ_D/D_m values in (a) $D_x = D_y$ and (b) $D_x \neq D_y$ cases (conventional HDMR).

the same as shown in Figs.7 and 13, respectively. Since the h value is relatively small, the information easily remains stable during AT writing as well as during 10 years of archiving.

Temperature T has a strong impact, since the T value is related to the $K_{ueff}(T)$ value and the denominator T in $K_{ueff}(T)V/(kT)$, and $K_{ueff}(T)V/(kT)$ is a variable in the exponential function of the dot error probability shown in Eq. (1). Therefore, $\partial T/\partial y$ is also a parameter with a strong impact. Figure 14 shows the h value needed to achieve a bER of 10^{-3} as a function of $\partial T/\partial y$ for various σ_D/D_m values in shingled HDMR. If the $\partial T/\partial y$ value is somewhat smaller than 14 K/nm, the h value increases considerably. If the $\partial T/\partial y$ values are the same, the h value to achieve a bER of 10^{-3} for $D_x = D_y$ is larger than that for $D_x \neq D_y$ because of the larger dot area variation. Figure 15 shows the result for conventional HDMR. Compared with the results in Figs. 14 and 15, the h value is more than doubled for shingled HDMR for the same $\partial T/\partial y$ value. To reduce the h value for conventional HDMR, it is necessary to increase the $\partial T/\partial y$ value considerably as shown in Fig. 15.

4. Conclusions

We examined the information degradation due to dot area variation and thermal fluctuation for 4 Tbpsi HDMR in terms of the following three factors.

(1) Reduction in readout field strength due to dot area variation

We considered that there are dependent $D_x = D_y$ and independent $D_x \neq D_y$ cases for the dot sizes D_x and D_y according to the dot manufacturing method. The bER value is smaller in $D_x \neq D_y$ case because of the smaller dot area variation.

To reduce the bER, it is necessary to manufacture dots with a small standard deviation σ_D/D_m less than about 20 % in $D_x = D_y$ case.

(2) Reversal of magnetization direction during 10 years of archiving due to thermal fluctuation

There is a minimum dot height h for a bER of 10^{-3}, which is determined by thermal fluctuation. The h value is relatively small as 4.2 nm for a mean dot size D_m of 6.4 nm and a σ_D/D_m of 20 % in $D_x = D_y$ case.

(3) Reversal of magnetization direction during adjacent track writing due to thermal fluctuation

If a thermal gradient $\partial T/\partial y$ of 14 K/nm in the cross-track direction can be achieved, the h value necessary

for adjacent track interference is also relatively small as 3.6 nm for shingled HDMR with a σ_D/D_m of 20 % in $D_x = D_y$ case. However, we need a very large $\partial T/\partial y$ value such as 18 K/nm to reduce the h value for conventional HDMR.

Acknowledgement We acknowledge the support of the Advanced Storage Research Consortium (ASRC), Japan.

References

1) S. H. Charap, P. -L. Lu, and Y. He: *IEEE Trans. Magn.*, **33**, 978 (1997).
2) F. Akagi, M. Mukoh, M. Mochizuki, J. Ushiyama, T. Matsumoto, and H. Miyamoto: *J. Magn. Magn. Mat.*, **324**, 309 (2012).
3) H. Yamane, S. J. Greaves, and Y. Tanaka: *IEEE Trans. Magn.,* **57**, 3200706-1-6 (2021).
4) T. Kobayashi, Y. Nakatani, and Y. Fujiwara: *J. Magn. Soc. Jpn.*, **46**, 10 (2022).
5) T. Kobayashi, Y. Nakatani, and Y. Fujiwara: *J. Magn. Soc. Jpn.*, **46**, 49 (2022).
6) T. Kobayashi, Y. Nakatani, and Y. Fujiwara: *J. Magn. Soc. Jpn.*, **47**, 1 (2023).
7) M. Mansuripur and M. F. Ruane: *IEEE Trans. Magn.*, **MAG-22**, 33 (1986).
8) J. -U. Thiele, K. R. Coffey, M. F. Toney, J. A. Hedstrom, and A. J. Kellock: *J. Appl. Phys.*, **91**, 6595 (2002).
9) T. Kobayashi, Y. Isowaki, and Y. Fujiwara: *J. Magn. Soc. Jpn.*, **39**, 8 (2015).
10) E. D. Boerner and H. N. Bertram: *IEEE Trans. Magn.*, **34**, 1678 (1998).

Received Jan. 18, 2023; Accepted Mar. 1, 2023

J. Magn. Soc. Jpn., **47**, 66-69 (2023) <Paper>

Method for Rapid Detection of Bacteria Using Magnetic Nanoparticle Aggregates

Y. Pu, H. Zhao*, T. Murayama**, L. Tonthat*, K. Okita**, Y. Watanabe**, S. Yabukami*, **
School of Engineering, Tohoku Univ., *6-6-05 Aramaki aza-aoba, Aoba-ku, Sendai 980-8579, Japan*
*Graduate school of Engineering, Tohoku Univ., *6-6-05 Aramaki aza-aoba, Aoba-ku, Sendai 980-8579, Japan*
**Graduate school of Biomedical Engineering, Tohoku Univ., *6-6-05 Aramaki aza-aoba, Aoba-ku, Sendai 980-8579, Japan*

A novel method for the rapid detection of bacteria in the liquid phase for point-of-care testing was developed using magnetic nanoparticles (MNPs) conjugated with antibodies. We utilized the magnetic characteristic that the magnetic susceptibility decreases when the magnetism of MNP aggregate changes from ferromagnetism to superparamagnetism after bacteria bind to MNPs through an antigen-antibody reaction (Nanomag-D, 500 nmϕ, 0.2 µl/sample). The magnetic susceptibility of *Fusobacterium nucleatum* samples was measured using a lab-made detection setup. We found that the susceptibility depends on the concentration of *Fusobacterium nucleatum* with optical density (OD) values ranging from 10^{-4} to 1 (i.e. $8 \times 10^4 \sim 8 \times 10^8$ CFU/ml). In addition, the detection time was only about 49 seconds, which shows promise for point-of-care testing.

Key words: Bacteria detection, Magnetic nanoparticle, Magnetic susceptibility, Antigen-antibody reaction, *Fusobacterium nucleatum*

1. Introduction

The threat of harmful bacteria and viruses has attracted the attention of people around the world, especially in the last three years due to the COVID-19 pandemic. Failure to promptly detect and treat such bacteria and viruses can lead to serious consequences for infected patients. As such, developing a more rapid and accurate detection method has become an important research topic. On the other hand, over the last few decades, there has been an increasing trend toward research of magnetic nanoparticles (MNPs) in biomedical field. Their properties have been demonstrated to be quite different compared to bulk materials such as high surface-to-volume ratio, and superior magnetic response [1]. Using these properties, MNPs can be applied in different areas such as magnetic hyperthermia, and biological substance detection [2)~5)]. To detect a specific type of bacteria, the MNPs are coated with detecting antibodies and these antibodies selectively capture the bacteria via antigen-antibody reactions. There are countless types of bacteria in the world with some of them being beneficial or harmful to humans. *Fusobacterium nucleatum* is a type of anaerobic bacteria about 1 µm in size and one of the resident species in the oral cavity and pharynx at the back of the mouth. It is generally regarded as a causative agent of gingivitis, periodontal disease, and colorectal cancer [6)]. By detecting such bacteria, patients can be forewarned about the risk of colorectal cancer and diseases related to the large intestine.

Currently, there are many detection methods such as polymerase chain reaction (PCR) [7)] and dielectrophoretic impedance measurement (DEPIM) [8)]. However, PCR takes at least a few hours and DEPIM requires a technician to operate. In our previous study, we proposed a rapid bacteria detection system with a detection time of about 15 minutes by utilizing the magnetic property changes of MNP-antigen-antibody aggregates under a switching DC magnetic field [4)].

In this study, for a simpler and quicker detection, we proposed a novel method of using the magnetic susceptibility of MNP-antigen-antibody aggregates under an AC magnetic field to detect *Fusobacterium nucleatum* for about 49 seconds. The susceptibility was found to be concentration dependence of *Fusobacterium nucleatum* with optical density (OD) values ranging from 10^{-4} to 1.

2. Design and Principle of Bacteria Detection System

2.1 Detection Principle

Fig. 1 shows the principle of bacteria detection. We used the magnetic characteristic that the magnetic susceptibility decreases when the magnetism of MNP aggregate changes from ferromagnetism to superparamagnetism, when bacteria are added and have antigen-antibody reaction with the MNPs. The reason is that when bacteria get into the aggregate of MNPs, the distance between the MNPs increases and the magnetic

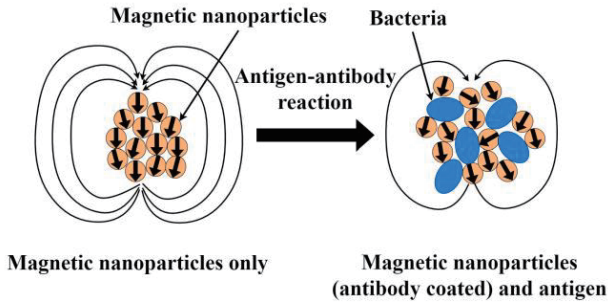

Fig. 1 Principle of bacteria detection.

Corresponding author:
Y. Pu (e-mail: pu.youcheng.r3@dc.tohoku.ac.jp).

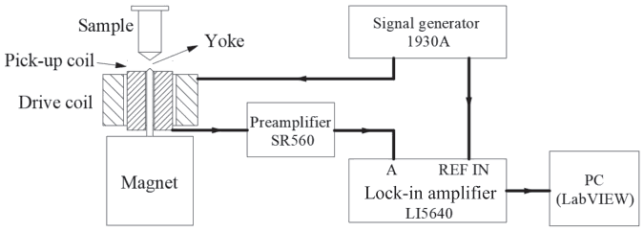

Fig. 2 Schematic view of constructed detection system.

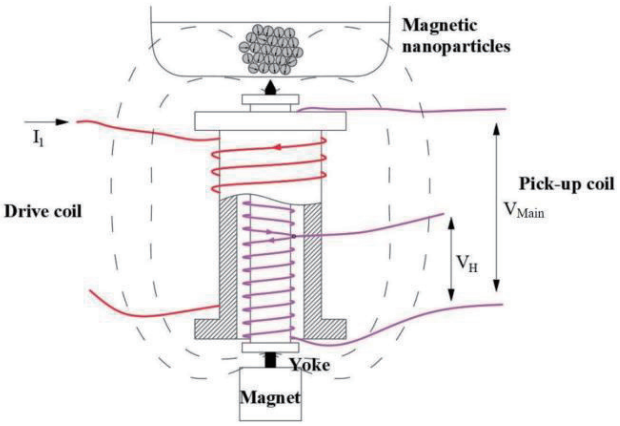

Fig. 3 Schematic view of detection device.

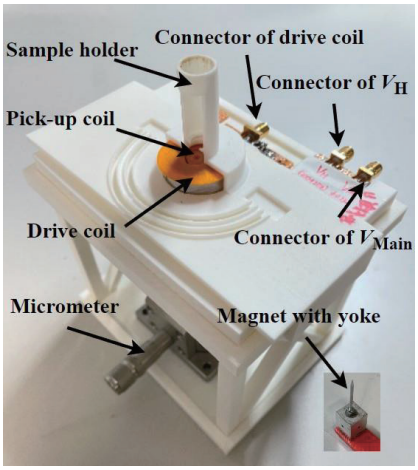

Fig. 4 Physical view of detection device.

coupling effect gets weakened. As a result, the magnetization of the aggregate becomes smaller leading to a decrease in the magnetic susceptibility. By utilizing this characteristic, we can detect *Fusobacterium nucleatum* by measuring the magnetic susceptibility of their MNP aggregate, which can be optimized by the voltage in a pick-up coil induced by the MNP aggregate and *Fusobacterium nucleatum*.

2.2 Design of Detection System and Experimental Setup

Fig. 2 shows the overall schematic view of the constructed detection system. It consists of the detection device (including a drive coil, a pick-up coil and a magnet yoke), a signal generator (AWG1005) which generates signals with a constant voltage of 200 mV and different frequencies of 0.31, 1.01, 3.01 and 10.01 kHz, a preamplifier (SR560) and a lock-in amplifier (LI5640, sensitivity was 1 μV and time constant was 300 ms). Fig. 3 shows the detailed schematic view of the detection device. The detection device is composed of a drive coil (400 turns, length of 10 mm, diameter of 9 mm), a differential pick-up coil (upper 200 turns and lower 200 turns reverse winding, length of 11 mm in total, diameter of 3.6 mm) and a magnet yoke. The drive coil is connected to a signal generator to apply a uniform magnetic field to the sample. After the sample is placed in the detection device, the change in magnetic field caused by the sample is measured as the induced voltage in the pick-up coil by Faraday's law of induction. Since the signal of the sample is too small, the differential structure of pick-up coil consisting of two identical reverse-wounded coils connected in series is used. The magnet yoke is used to gather the MNPs to form an aggregate to improve detection accuracy and magnetize the MNP aggregate. V_H and V_{Main} are the measured voltages induced by the applied magnetic field and the magnetization of the MNP aggregate, respectively. Fig. 4 shows the physical view of the detection device. It mainly consists of drive and pick-up coils, a sample holder, an input connector of drive coil (connected to signal generator), two output connectors of V_H and V_{Main} and a micrometer for fine-tuning the relative position between pick-up and drive coils.

2.3 Optimization of Magnetic Susceptibility and Detection Procedure

Fig. 5 shows the flow chart of the detection procedure. First, the detection device is connected to the other devices, i.e. the connectors of drive coil and V_{Main} are connected to the signal generator and the preamplifier, respectively. The lock-in amplifier is connected to the preamplifier, the signal generator and the PC. The

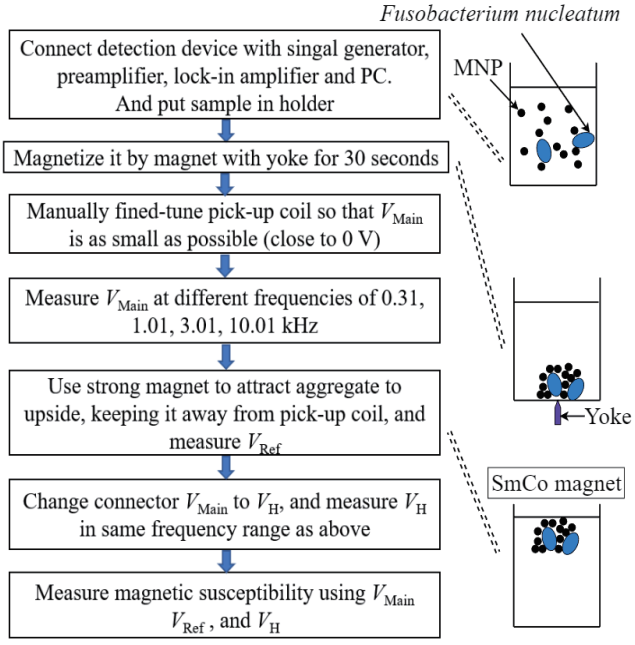

Fig. 5 Flow chart of detection procedure.

sample is then placed in the holder and magnetized by magnet yoke for 30 seconds. Then manually fined-tune the pick-up coil using the micrometer so that the voltage (i.e. V_{Main}) induced by the magnetized sample is as small as possible (close to 0 V) to improve the measurement sensitivity. The reason for doing this is that the change in voltage with and without aggregate at the microtube bottom is very small. V_{Main} is measured at different frequencies of 0.31, 1.01, 3.01 and 10.01 kHz. As for the applied magnetic field intensity, the measured V_H at four frequencies (0.31, 1.01, 3.01 and 10.01 kHz), were 0.014, 0.047, 0.14 and 0.67 V, respectively. As such, the respective intensities were calculated as 2.858, 2.867, 2.968 and 4.175 kA/m. Afterwards, a strong SmCo magnet (50 mm × 50 mm × 10 mm) is used to draw the aggregate to the top of the sample solution away from the pick-up coil, and V_{Ref} is measured at that time. Finally, switch the connection to the preamplifier from "connector of V_{Main}" to "connector of V_H", and measure V_H at the same frequencies as mentioned above. The susceptibility (χ) of MNP aggregate is calculated by Equation (1). The relationships between the magnetization (M), strength of applied magnetic field (H), and the measured voltages are shown by Equations (2) and (3) [9].

$$\chi = \frac{M_{Main} - M_{Ref}}{H} = \frac{1}{c} \cdot \frac{V_{Main} - V_{Ref}}{V_H} \quad (1)$$

$$M_{Main} - M_{Ref} = \frac{V_{Main} - V_{Ref}}{2\pi f \mu_0 n S_{coil} c} \quad (2)$$

$$H = \frac{V_H}{2\pi f \mu_0 n S_{coil}} \quad (3)$$

where c the ratio between the aggregate cross-sectional area (S_{sample}) and the cross-sectional area of one side of the differential pick-up coil (S_{coil}), μ_0 vacuum permeability, f frequency of applied field, n the number of turns. For the aggregate used in our experiment, the cross-sectional area of the aggregate is considered to be approximately constant with a diameter of about 1.7 mm. When there is the aggregate (MNPs and bacteria) at the bottom of the microtube, the induced voltage is measured as V_{Main}. After drawing the aggregate to the top of the solution away from the pick-up coil using the SmCo magnet, the induced voltage is measured again as V_{Ref}. In addition to signal component of the aggregate, V_{Main} includes the other components such as the solution and sample tube, as such the value of V_{Ref} was subtracted from the value of V_{Main}.

2.4 Sample Preparation of *Fusobacterium nucleatum*

The MNPs used for sample preparation are capable of antigen-antibody reaction with *Fusobacterium nucleatum* and can form aggregate using a yoke-equipped magnet. As such, the MNPs (Nanomag-D, 500 nmϕ, 0.2 µl/sample) were first coated by primary antibody (rabbit anti-*Fusobacterium nucleatum* ANT0084, 0.01 µL/sample). The antigen-antibody reaction time was 30 minutes to obtain a sufficient reaction. The 500 nm diameter for MNPs was optimized for the size of *Fusobacterium nucleatum* which is about 1 µm [4]. Six samples were prepared in total. There was no *Fusobacterium nucleatum* in sample 1, thus its OD value was 0. The OD values of the samples 2-6 were 10^{-4}, 10^{-3}, 10^{-2}, 10^{-1} and 1, respectively. Here, the OD value of 10^{-4} roughly corresponded to 8×10^4 CFU/ml.

3. Experiment Results and Discussion

Using the constructed detection system, the detection time was about 49 seconds (including pretreatment). Here, the pretreatment included sample agitation for 5 seconds using a vortex mixer and aggregation using a yoke-equipped magnet for 30 seconds. The detection was 2 seconds each for the detection of V_{Main} and V_{Ref}, and 10 seconds for the attraction of aggregate with a strong magnet.

Figs. 6 (a), (b), (c), (d), (e) and (f) show the experiment results for complex magnetic susceptibility of the sample aggregate with OD values of 0, 10^{-4}, 10^{-3}, 10^{-2}, 10^{-1} and 1 at different frequencies of 0.31, 1.01, 3.01 and 10.01 kHz. The dark blue line is the real part and red line is the imaginary part of complex susceptibility. The experiments were repeated 4 times for reproducibility and the average and standard deviation of the values were plotted. As shown in Fig. 6, a decreasing trend of the real part of susceptibility with increasing frequency was observed for all samples. This decreasing trend basically matches with the frequency dependence trend of the Debye model and the Fokker-Planck equation for AC susceptibility [10]. It was also observed that the imaginary part of susceptibility was around 0 for all samples below 3.01 kHz and increased from 3.01 kHz. This indicates that the phase of the magnetic susceptibility increased with increasing frequency, because not only the real part decreased, but the imaginary part also tended to increase slightly. As a result, the phase of magnetic susceptibility increased whereas the absolute value of magnetic susceptibility decreased. The reason for this phenomenon could be the resonance of the coils or the ferromagnetic resonance of the sample aggregate.

Fig. 7 shows the concentration dependence of real part of susceptibility of *Fusobacterium nucleatum* at different frequencies using the data in Fig. 6. It is clear that the real part of magnetic susceptibility showed decreasing trend at all frequencies observed as the OD value of the sample increased. It is considered that when *Fusobacterium nucleatum* gets into the aggregate of MNPs, the distance between MNPs increases, causing the magnetic coupling effect to weaken, thereby reducing the magnetization of the aggregate and the magnetic susceptibility. The error bars were larger than expected, future work will focus on improving the SN ratio of the detection system. Moreover, the miniaturization of the

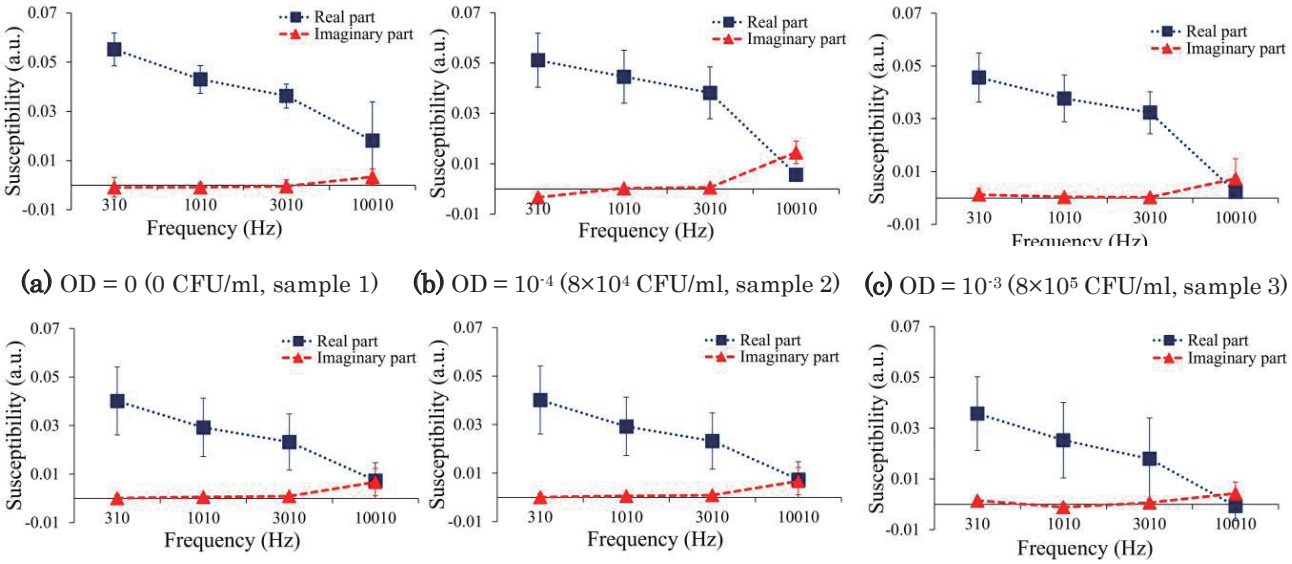

(a) OD = 0 (0 CFU/ml, sample 1) (b) OD = 10^{-4} (8×10^{4} CFU/ml, sample 2) (c) OD = 10^{-3} (8×10^{5} CFU/ml, sample 3)

(d) OD = 10^{-2} (8×10^{6} CFU/ml, sample 4) (e) OD = 10^{-1} (8×10^{7} CFU/ml, sample 5) (f) OD = 1 (8×10^{8} CFU/ml, sample 6)

Fig. 6 Experiment results for magnetic susceptibility of sample aggregate for OD values of 0, 10^{-4}, 10^{-3}, 10^{-2}, 10^{-1}, 1 (number of trials = 4).

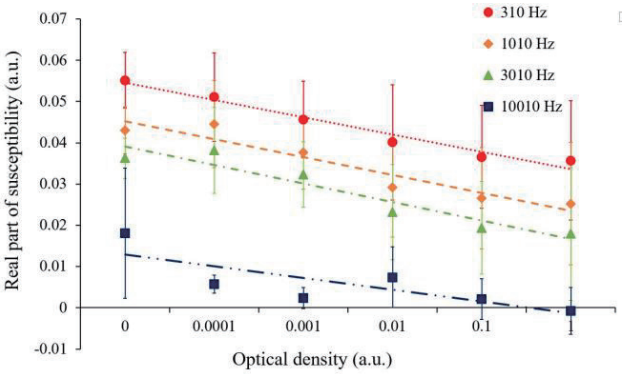

Fig. 7 Concentration dependence for real part of magnetic susceptibility of *Fusobacterium nucleatum* (number of trials = 4).

detection system and the addition of more detection points will be addressed in the future.

4. Conclusions

1. A novel method for simple and rapid detection of *Fusobacterium nucleatum* was developed using MNPs conjugated with anti-*Fusobacterium nucleatum* antibodies.
2. The concentration dependence of real part of magnetic susceptibility of *Fusobacterium nucleatum* was found between OD values of 10^{-4} and 1 (8×10^{4}~8×10^{8} CFU/ml).
3. When the concentration of *Fusobacterium nucleatum* increased, the magnetic susceptibility of the aggregate of MNPs and *Fusobacterium nucleatum* decreased.
4. The detection time was about 49 seconds (including pretreatment), which was significantly faster than other methods.

Acknowledgments I would like to thank Professor N. Takahashi and J. Washio for cultivating *Fusobacterium nucleatum*. This work was supported in part by the Center of Innovative Science and Technology-based Radical Innovation and Entrepreneurship Program (COI STREAM), and the Adaptable and Seamless Technology Transfer Program (A-STEP) from the Japan Science and Technology Agency (JST), AMED (JP21zf0127001), and the Frontier Research Institute for Interdisciplinary Sciences at Tohoku University.

References

1) A. H. Lu, E. L. Salabas, and F. Schüth: *Angew. Chem. Int. Ed.*, **46**, 1222 (2007).
2) A. Shikano, L. Tonthat, A. Kuwahata, et al: *T. Magn. Soc. Jpn. (Special Issues)*, **6**, 100 (2022).
3) L. Tonthat, S. Takahashi, H. Onodera, et al: *AIP Adv.*, **9**, 125325 (2019).
4) S. Yabukami, T. Murayama, S. Takahashi, et al: *IEEE Trans. Magn.*, **58**, 6100305 (2022).
5) T. Yoneyama, A. Kuwahata, T. Murayama, et al: *IEEE Trans. Magn.*, **58**, 5300406 (2022).
6) T. Ohkusa: *J. Microbiol.*, **27**, 169 (2013).
7) R.K. Saiki, S. Scharf, F. Faloona, et al: *Science*, **230**, 1350 (1985).
8) J Suehiro, R Hamada, D Noutomi, et al: *J. Electrost.*, **57**, 157 (2003).
9) V. Concord, B. Mehdaoui: *Rev. Sci. Instrum.*, **85**, 093904 (2014).
10) Z. Du, Y. Cui, Y. Sun, et al: *IEEE Trans. Nanobioscience*, **21**, 496 (2022).

Received Nov. 14, 2022; Accepted Jan. 19, 2023

J. Magn. Soc. Jpn., **47**, 70-77 (2023) <Paper>

Development of Electromagnetic Levitation System for Thin Steel Plates with Electromagnets and Permanent Magnets for Levitation Support (Experimental Consideration of Vibration Characteristics of Levitated Steel Plates)

S. Kayama, Y. Ichikawa, T. Nagayoshi, S. Kawamura, K. Ogawa, D. Uchino,

K. Ikeda*, T. Kato**, A. Endo***, T. Narita, and H. Kato

Tokai University, 4-1-1 Kitakaname, Hiratsuka-shi, Kanagawa 259-1292, Japan
**Hokkaido University of Science, 7-15-4-1 Maeda, Teine-ku, Sapporo-shi, Hokkaido 006-8585, Japan*
***Tokyo University of Technology, 1404-1 Katakura-cho, Hachiouji-shi, Tokyo 192-0982, Japan*
****Fukuoka Institute of Technology., 3-30-1 Wajirohigashi, Higashi-ku, Fukuoka-shi, Fukuoka 811-0295, Japan*

Contact conveyance by rollers is used in thin steel-plate production lines, and scratches on the surface of the plates and plating defects may occur. Therefore, noncontact magnetic levitation conveyance of thin steel plates using the attractive force of electromagnets has been proposed. We previously studied a magnetic levitation system for thin steel plates using both electromagnets and permanent magnets. However, the vibration characteristics of levitated steel plates have not yet been studied. In this study, magnetic levitation experiments were conducted on steel plates using the optimum arrangement of permanent magnets for each condition obtained by the genetic algorithm, and the stability of levitation was experimentally investigated. The results confirmed that the levitation performance of the steel plates was different for each gap. As the gap increased and approached the optimum gap obtained in the GA search, the attractive force of the permanent magnet became appropriate for assisting levitation. This optimized arrangement of permanent magnets reduces the deflection of the levitated steel plate, and the vibration could be suppressed. Thus, the proposed method can change the vibration characteristics of a levitated steel plate and improve levitation stability.

Keywords: electromagnetic levitation control, thin steel plate, permanent magnet, electromagnet, genetic algorithm

1. Introduction

Thin steel plates, which are widely used in industrial products, are transported via contact with rollers during the manufacturing process. Contact conveying causes scratches and peeling of the plating layer on the surface of thin steel plates. In recent years, noncontact conveying has been actively studied as a solution[1)-4)]. Our research group has proposed a magnetic levitation system for thin rectangular steel plates using the attractive force of electromagnets[5)]. However, magnetic levitation using electromagnets alone incurs an increased cost owing to the increase in the number of electromagnets required for larger thin steel plates. Furthermore, it also incurs the problem of complex vibration caused by the deflection of levitated flexible thin steel plates in areas where the attractive force of the electromagnets is not applied adversely affecting the levitation performance. To solve these problems, we are studying a hybrid magnetic levitation system in which permanent magnets are evenly installed in locations where the attractive force of electromagnets is not applied, aiming to stabilize levitation[6)]. Permanent magnets are used in various devices, such as motors, because of their ability to generate a steady magnetic field once magnetized. Zero-power control using permanent magnets to generate a bias magnetic flux for levitation support has been proposed[7)] and is currently being studied[8)]. This research group used permanent magnets to assist in the levitation of electromagnets. The deflection of the steel plate was suppressed by arranging permanent magnets at equal intervals around the levitating electromagnets, thereby improving levitation stability. However, to obtain higher levitation stability, multiple parameters, such as the number and arrangement of permanent magnets, need to be optimized. The optimal permanent magnet configuration is difficult to obtain experimentally because of the large number of combinations of these parameters. Therefore, the research group focused on genetic algorithms (hereafter referred to as GAs), which are optimization algorithms. Using a GA, we determined an arrangement of permanent magnets for levitation supports that can best suppress the deflection of steel plates, performed levitation experiments using the obtained arrangement, and confirmed that the levitation stability of the steel plates was improved[9)]. We determined the optimum arrangement of permanent magnets in a steel plate levitated by applying tension from the horizontal direction using a GA, conducted levi-

Corresponding author: T. Narita
(e-mail: narita@tsc.u-tokai.ac.jp).

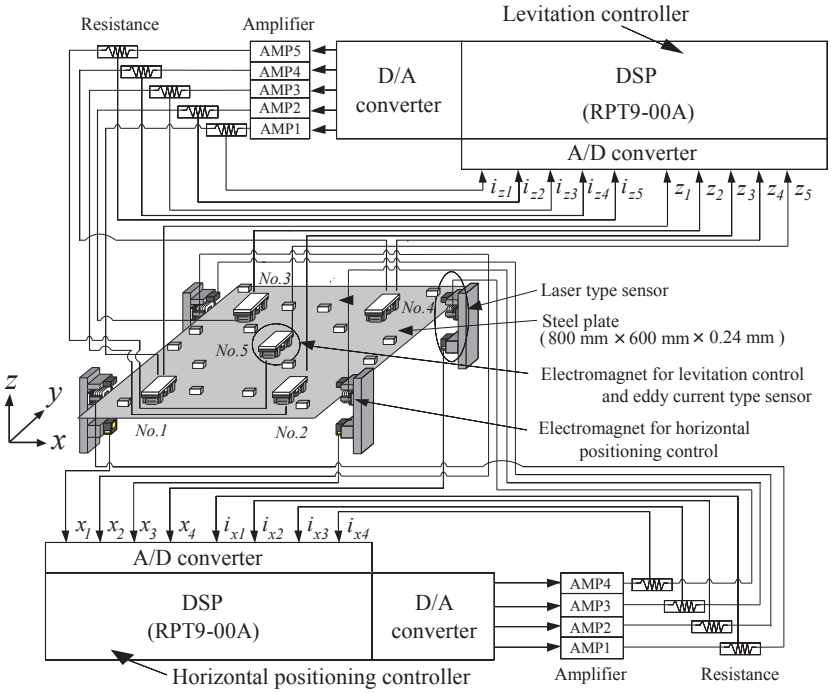

Fig. 1 Outline of electromagnetic levitation control system with permanent magnets.

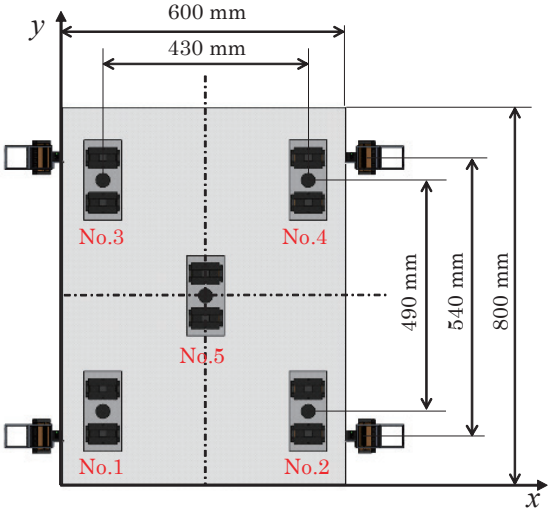

Fig. 2 Top view of arrangement of electromagnets.

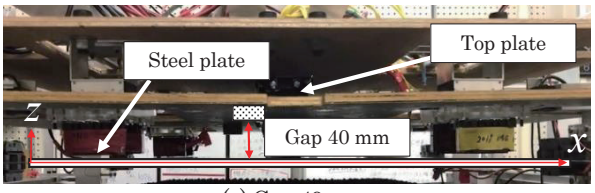

(a) Gap 40 mm

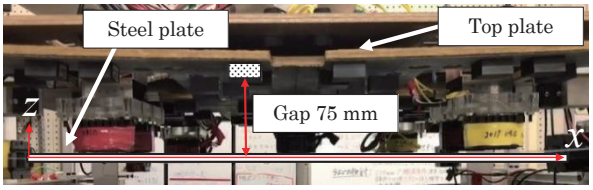

(b) Gap 75 mm

Fig. 3 Side view of gaps.

tation experiments and confirmed that deflection can be suppressed. Comparing to previous study without horizontal electromagnets, the optimized arrangement of permanent magnet considering of the horizontal electromagnets could suppress the deflection of the steel plate and reduce the number of permanent magnets[10]. Furthermore, we determined the optimum arrangement of permanent magnets when the distance between the permanent magnet surface and the steel plate was changed, and the position of tension applied from the horizontal direction was changed[11] using a GA. However, studies on the vibration characteristics of levitated steel plates with applied magnetic fields generated by horizontal and vertical electromagnets and permanent magnets for levitation support have not yet been conducted. In this study, magnetic levitation experiments of steel plates were conducted using the optimum arrangement of permanent magnets for each condition obtained using a GA when the distance between the permanent magnets and steel plates was changed, and the stability of levitation was experimentally investigated.

2. Magnetic levitation system using both electromagnets and permanent magnets

2.1 Overview of magnetic levitation system using both electromagnets and permanent magnets

Fig. 1 shows the schematic of the hybrid magnetic levitation system. The surfacing object was a rectangular galvanized steel plate (SS400) with a length of 800 mm, a width of 600 mm, and a thickness of 0.24 mm. Electromagnet units were installed at five locations abo-

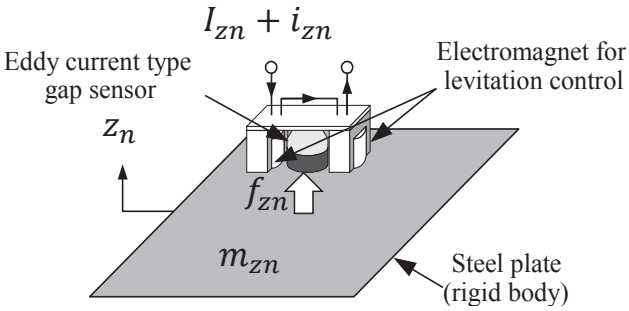

Fig. 4 Theoretical model of levitation control of steel plate.

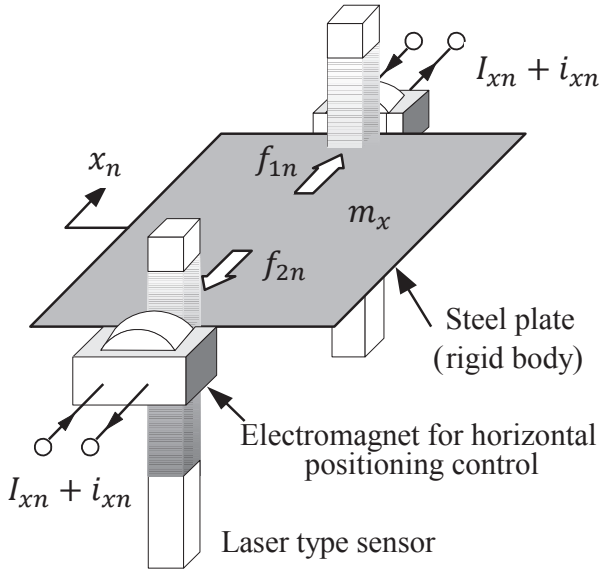

Fig. 5 Theoretical model of horizontal positioning control of steel plate.

ve the steel plate, and the levitation was controlled such that the distance between the electromagnet surface and the steel plate surface was 5 mm by the attractive force of each unit. A detailed view of the levitation electromagnet unit is shown in Fig. 2. The levitation electromagnet unit consists of two electromagnets sandwiched between two eddy-current noncontact displacement sensors that measure the displacement of the steel plate. A schematic of the horizontal positioning control system is shown in the lower part of Fig. 1. A horizontal electromagnet unit consisting of an electromagnet and a transmission laser displacement sensor was installed near the longitudinal edge of the steel plate at four opposing locations, and positioning control was performed such that the distance between the electromagnet surface and the edge of the steel plate was 5 mm. Preliminary experiments confirmed that noise from the sensor did not affect the measurement results. The levitation and horizontal directional electromagnet units were installed, as shown in Fig. 2, with the distance between the centers of the horizontal directional electromagnets set at 540 mm. In this study, experiments were conducted in a stationary state for a basic study of the proposed system. An SS400 top plate (0.5 mm thickness) was placed around the levitation electromagnet unit, and several ferrite magnets (30 mm × 30 mm × 15 mm, surface magnetic flux density 0.12 T) were placed on the top plate to assist levitation, as shown in Fig. 1. The poles of the permanent magnets were arranged such that the steel plate side consisted of N poles. The top plate can be moved up and down as shown in Fig. 3, and the distance between the surface of the permanent magnet and the steel plate (hereinafter referred to as the "gap") can be changed without changing the levitation height of the levitation control electromagnet.

2.2 Control model and control system design for magnetic levitation systems

To control the five magnets independently, the system divides the steel plate into five virtual masses, each of which is modeled as a concentrated constant system, as shown in Fig. 4. An equilibrium state exists, in which the steel plate is maintained at a certain distance if it is supported by a static attractive force from an electromagnet. If the vertical displacement from this point is z_n (subscript n corresponds to Nos. 1 to 5 in Fig. 1), the equations of motion are expressed as follows:

$$m_{zn}\ddot{z}_n = 2f_{zn}, \tag{1}$$

where m_{zn} is the mass of steel plate m divided virtually into five parts (but considering the effect of the attractive force of permanent magnets) [kg], and f_{zn} is the variation value of the attractive force per electromagnet [N]. The following equation of state is obtained by adopting the displacement z_n, velocity $\dot{z}_n$, and electromagnetic coil current i_{zn} of the steel plate as state variables for the equation of electromagnetic attractive force and electromagnetic coil current, which are linearized approximations, as in the previous report.

$$\dot{\boldsymbol{z}}_{\boldsymbol{n}} = \boldsymbol{A}_{\boldsymbol{zn}}\boldsymbol{z}_{\boldsymbol{n}} + \boldsymbol{B}_{\boldsymbol{zn}}v_{zn}, \tag{2}$$

$$\boldsymbol{z}_{\boldsymbol{n}} = [z_n \quad \dot{z}_n \quad i_{zn}]^{\mathrm{T}}$$

$$A_{zn} = \begin{bmatrix} 0 & 1 & 0 \\ \dfrac{2F_{zn}}{m_{zn}Z_0} & 0 & \dfrac{2F_{zn}}{m_{zn}I_{zn}} \\ 0 & -\dfrac{L_{zeff}}{L_z}\cdot\dfrac{I_{zn}}{Z_0^2} & -\dfrac{R_z}{2L_z} \end{bmatrix}$$

$$B_{zn} = \begin{bmatrix} 0 & 0 & \dfrac{1}{2L_z} \end{bmatrix}^{\mathrm{T}}$$

where F_{zn} is the total static attractive force generated by a pair of electromagnets in the equilibrium levitation state [N], Z_0 is the gap between the surfaces of the

electromagnet and steel plate in the equilibrium levitation state [m], I_{zn} is the steady-state current value of the electromagnet coils in the equilibrium levitation state [A], i_{zn} is the variation value from the steady-state current of the electromagnet coils [A], L_z is the inductance per electromagnet coil in the equilibrium levitation state [H], R_z is the total resistance of the pair of electromagnet coils [Ω], v_{zn} is the variation from the steady-state voltage of the electromagnet coil [V], L_{zeff}/Z_0 is a constant corresponding to the effective flux per electromagnet [H], and L_{zlea} is the leakage flux per electromagnet [H]. As the control system is configured as a discrete-time system, the optimal control law is obtained based on the optimal control theory for discrete-time systems[12]. The evaluation function for discrete-time systems is expressed as follows:

$$J_{zd} = \sum_{k=0}^{\infty} \left[\boldsymbol{z}_d(k)^{\mathrm{T}} \boldsymbol{Q}_{zd} \boldsymbol{z}_d(k) + v_{zd}(k)^{\mathrm{T}} r_{zd} v_{zd}(k) \right], \quad (3)$$

where $\boldsymbol{Q}_{zd}$ is a matrix, whose elements are weight coefficients for the levitation displacement z_d, velocity $\dot{z}_d$, and current i_{zd}; r_{zd} is a weight coefficient for the control input v_{zd}; and the control law F_{zn} was determined to minimize J_{zd}. With state feedback, the control input v_{zn} is expressed as follows:

$$v_{zn} = -\boldsymbol{F}_{zn} \boldsymbol{z}_n. \quad (4)$$

2.3 Horizontal positioning control system

As shown in Fig. 5, the horizontal motion was modeled as a 1-DOF system moving along only one axis. Therefore, it is assumed that the two electromagnets placed on one side of the steel plate generate the same attractive force. Upon placing one electromagnet on each of the two opposite sides of the steel plate and applying the same static attractive force, the steel plate is in equilibrium, and the equation of motion in the horizontal direction owing to small changes in the steel plate from that state is expressed as follows:

$$m_x \ddot{x}_n = f_{1n} - f_{2n} = f_{xn}, \quad (5)$$

where m_x is the mass of steel plate m divided virtually into two parts [kg], f_{1n}, f_{2n} are the variation value of the attractive force per electromagnet [N] and f_{xn} is the total variation value of the attractive force of electromagnet. The following equation of state is obtained by arranging the attractive force equation and the circuit equation with linearized approximation, as in Section 2.2, and considering the horizontal displacement $\boldsymbol{x}_n$ of the steel plate, the velocity $\dot{\boldsymbol{x}}_n$, and the variation value of the coil current i_{xn} as state variables.

$$\dot{\boldsymbol{x}}_n = \boldsymbol{A}_{xn} \boldsymbol{x}_n + \boldsymbol{B}_{xn} v_{xn}, \quad (6)$$

$$\boldsymbol{x}_n = [x_n \quad \dot{x}_n \quad i_{xn}]^{\mathrm{T}}$$

$$A_{xn} = \begin{bmatrix} 0 & 1 & 0 \\ \dfrac{4F_{xn}}{m_{xn}X_0} & 0 & \dfrac{4F_{xn}}{m_{xn}I_{xn}} \\ 0 & -\dfrac{L_{xeff}}{L_x} \cdot \dfrac{I_{xn}}{X_0^2} & -\dfrac{R_x}{2L_x} \end{bmatrix}$$

$$B_{xn} = \begin{bmatrix} 0 & 0 & \dfrac{1}{2L_x} \end{bmatrix}^{\mathrm{T}}$$

where F_{xn} is the static attractive force [N], X_0 is the gap between the surfaces of the electromagnet and steel plate in equilibrium levitation [m], I_{xn} is the steady-state current value to obtain a static attractive force [A], L_x is the inductance of the electromagnet coils in equilibrium levitation [H], R_x is the total resistance value of two electromagnet coils [Ω], v_x is the variation value from the steady-state voltage applied to the electromagnet coils [V], L_{xeff}/X_0 is a constant corresponding to the effective flux of the electromagnet [H], and L_{xlea} is a constant corresponding to the flux leakage of the electromagnet [H]. The optimal control law for the horizontal direction was obtained in the same manner as for the ascending direction. The evaluation function for the discrete-time system is expressed as follows:

$$J_{xd} = \sum_{k=0}^{\infty} \left[\boldsymbol{x}_d(k)^{\mathrm{T}} \boldsymbol{Q}_{xd} \boldsymbol{x}_d(k) + v_{xd}(k)^{\mathrm{T}} r_{xd} v_{xd}(k) \right], \quad (7)$$

where $\mathbf{Q}_{xd}$ is a matrix, whose elements are weight coefficients for the horizontal displacement x_d, velocity v_d, and current i_{xd}; r_{xd} is a weight coefficient for the control input v_{xd}; and the control law F_{xn} is determined to minimize J_{xd}. With state feedback, the control input v_{xn} is expressed as follows:

$$v_{xn} = -\boldsymbol{F}_{xn} \boldsymbol{x}_n. \quad (8).$$

3. Determination of the optimal arrangement of permanent magnets for levitation support

3.1 Shape analysis of steel plate in surfacing

In this system, the attractive force of permanent magnets is applied to areas where the attractive force of electromagnets is not applied, thereby suppressing the deflection of thin steel plates during levitation and improving the levitation stability. Therefore, the shape of a thin steel plate during levitation, when the attractive force of the permanent magnet is applied, is determined by analysis. The attractive force generated by the

permanent magnet on the steel plate was previously reported[10]. The equation for the static deflection of a thin steel plate under the action of gravity and the attractive force of permanent magnets is expressed as follows:

$$D\nabla^4 z = f_z + f_x \frac{\partial^2}{\partial x^2} z + f_{PM} - \rho h g. \quad (9)$$

where f_z is the external force applied in the vertical direction per unit area of a thin steel plate by a horizontal electromagnet [N/m^2]; f_x is the external force applied in the horizontal direction per unit area of a thin steel plate by a horizontal electromagnet [N/m]; f_{PM} is the attractive force per unit area applied to a thin steel plate from the vertical direction by an installed permanent magnet [N/m^2]; ρ is the density of a thin steel plate [kg/m^3]; h is the thickness of steel plate[m]; and g is the acceleration of gravity [m/s^2].

3.2 Evaluation value

To determine the optimal number and arrangement of permanent magnets and the gap that effectively suppresses the deflection of a thin steel plate, an evaluation value was set based on the shape of the steel plate to which the attractive force from the permanent magnets was applied by differential analysis. In this study, the evaluation value J obtained from the evaluation function in eq. (10) was used, which was defined in the same way as in previous reports[10].

$$J = \frac{J_Z}{J_{Z_0}} \times W_Z + \frac{J_D}{J_{D_0}} \times W_D \quad (10)$$

$$W_Z = W_D = 0.5$$

Where J_Z is root means square of the deflection of the steel plate. J_D is the maximum deflection of the steel plate. J_{Z0} and J_{D0} are defined as J_Z and J_D when permanent magnets are not installed. The evaluated value J is 1 when only electromagnets are installed; the lower the value, the more effective the suppression of deflection. W_Z and W_D are the weight coefficients for the average and maximum deflections, respectively, and are set to 0.5.

3.3 Determination of the optimal arrangement of permanent magnets using genetic algorithm

As the attractive force of permanent magnets varies with the gap, the optimal number and arrangement of permanent magnets were optimized to suppress the deflection of thin steel plates effectively at each gap. However, the determination of the optimal values experimentally is difficult because of the large number of search patterns. The optimal permanent magnet configuration was determined via the GA, an optimization algorithm, using the same method as previously reported[10]. In this algorithm, effect from electromagnets to attractive force generated by permanent magnets did not consider, based on previous study[13]. Table 1 lists the search conditions. In this study, the calculation was terminated when the final value of the evaluation function remained unchanged for 300 generations. As search conditions, the steady-state current value of the horizontal electromagnets was set to 0.5 A, the search range of the gap was set from 40 mm to 75 mm, and the increment value was set to 5 mm to determine the optimal arrangement of permanent magnets. The optimized arrangement of permanent magnets, the number of permanent magnets installed, steel plate geometry, and GA-derived evaluation value J for each gap are shown in Fig. 6. This figure shows that the arrangement and number of permanent magnets are different for each gap, and the shape of the steel plate is also different for each gap. The minimum number of permanent magnets were 4 and the maximum was 56. When the gap is small, the attractive force generated by a permanent magnet is large; thus, the number of magnets is small. When the gap is large, the attractive force generated is small relative to the distance; therefore, the number of magnets increases. This confirms that, when the gap is small, the number of permanent magnets that can be installed is small and the deflection of the steel plate shape is locally larger at the point where the permanent magnets are installed. As the gap increases and the number of permanent magnets that can be installed increases, local deflection owing to the permanent magnets is no longer observed, and a flat steel plate shape with little deflection can be obtained. The optimized evaluated value J for each gap is shown in Fig. 7. This figure shows that the lowest value of J was obtained when the gap was 70 mm, with a value of J = 0.040562.

Table 1 Search conditions.

Parameter	Value
Number of genes	32
Number of consecutive generations	300
Crossover method	Uniform crossing
Crossover rate	90%
Mutation rate	1%
Gap	40-75 mm

4. Experiments on the magnetic levitation of thin steel plates using an optimal arrangement of permanent magnets

4.1 Experimental conditions

Magnetic levitation experiments on steel plates were performed using an optimized arrangement of permanent magnets for each gap, as described in Section 3. As in the GA search, the steady-state current of the horizontal electromagnets was set to 0.5 A. Levitation experiments were conducted for each gap using the

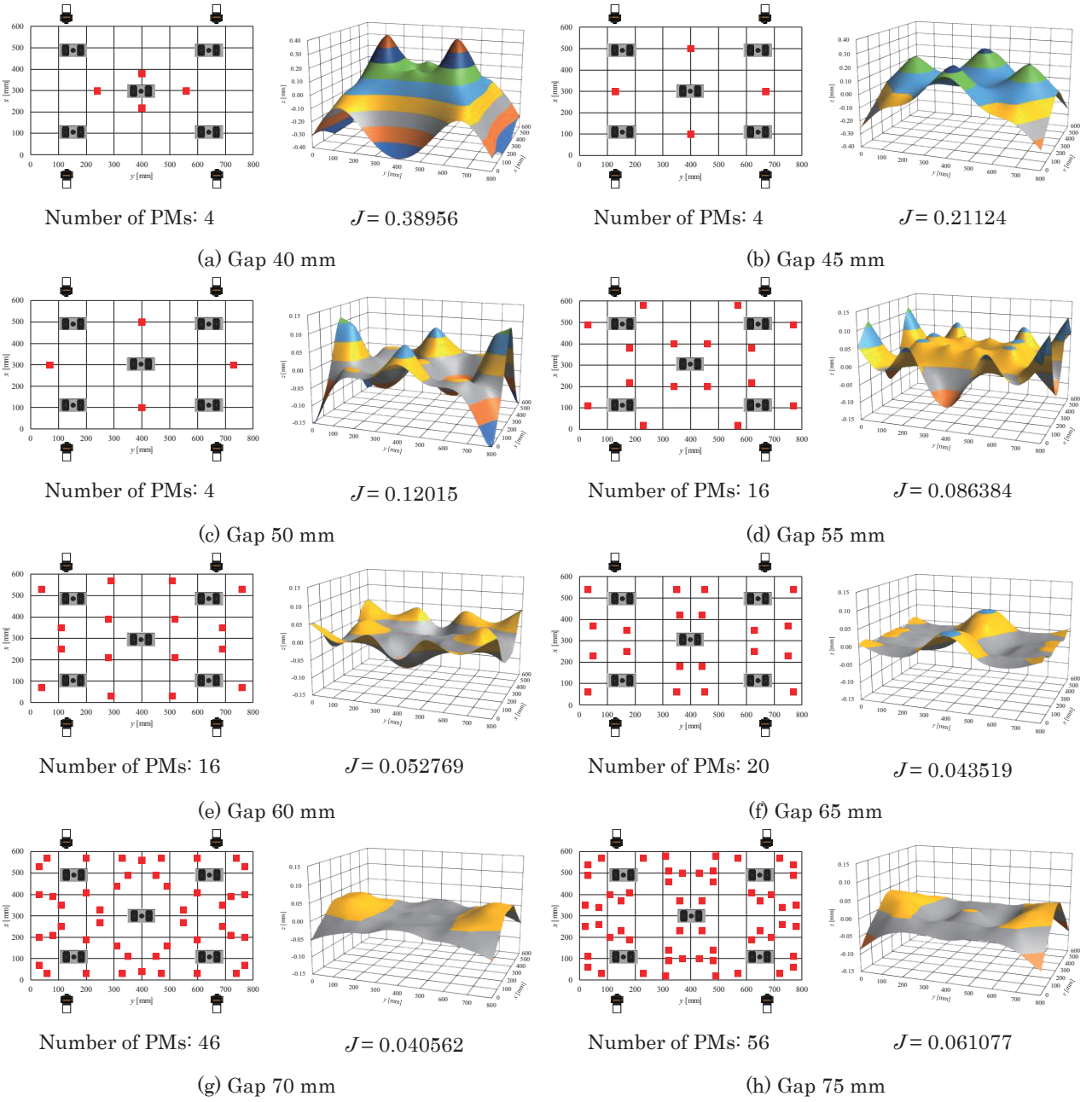

Fig. 6 Optimized arrangement of permanent magnets and plate shape at each gap.

permanent magnet arrangement shown in Fig. 6, and the vibration of the steel plate was measured for 15 s using an eddy-current noncontact displacement sensor at electromagnet unit No. 5 in Fig. 2. Tables 2 and 3 list the parameters of the weight coefficients used in Eqs. (3) and (7) to obtain the feedback gains in this experiment.

4.2 Experimental results

The Fig. 8 shows the vibration spectrum of the steel plate in the vertical direction and the displacement standard deviation (STD) of the steel plate measured by the eddy-current noncontact displacement sensor of electromagnet unit No. 5 in Fig. 2 during the levitation experiment at each gap. STD of displacement was calculated using eq. (11).

$$STD = \frac{\sum_{i=1}^{N} \sqrt{(x_i - \bar{x})^2}}{N}, \tag{11}$$

where N denotes the number of data points, x_i denotes the displacement of the i th point, and $\bar{x}$ denotes the displacement of the control point. The vibration spectra of the steel plate at each gap appeared at 0–10 Hz. This range was the natural frequency of the elastic vibration in the x and y directions. In the case of the gap of 40 mm shown in Fig. 8(a) with the narrowest condition in this study, the vibration of the steel plate is not suppressed. The waveform of the vibration spectrum became smaller as the gap increased, that is, as the number of installed permanent magnets increased, with the waveform of the

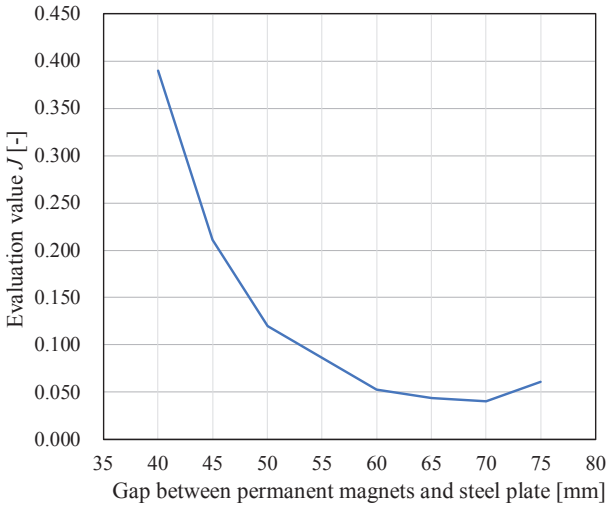

Fig. 7 Evaluation value J at each gap between permanent magnets and steel plate.

Table 2 Weighting coefficients in z (levitation) direction.

Parameter	Value
$\mathbf{Q}_{zd}$	diag(1.5×10^{5}, 5.0×10^{-2}, 1.0×10^{2})
r_{zd}	1.0×10^{-1}

Table 3 Weighting coefficients in the x (horizontal) direction.

Parameter	Value
$\mathbf{Q}_{xd}$	diag(1.90×10^{7},5.0×10^{-10}, 6.0×10^{-7})
r_{xd}	$3.0\times10^{-0.7}$

spectrum being the smallest at a gap of 65 mm. The spectral waveform became larger when the gap was larger than 65 mm. The STD value was also the lowest at a gap of 65 mm. Based on these results, we consider 65 mm to be the optimum gap value for the levitation experiment. When the gap is small, the attractive force of the permanent magnets acts on the steel plate to a large extent, which is believed to have caused the plate to vibrate. Consequently, the waveform of the vibration spectrum was considered to be larger. As the gap increased and approached the optimum gap obtained in the GA search, the pull force of the permanent magnet became appropriate for assisting levitation, and the vibration of the steel plate was suppressed. As the gap increased, the attractive force generated by one permanent magnet decreased. Using the reduced attractive force according to the wide gap, the optimum arrangement in which permanent magnets distributed the whole area of the steel plate could be obtained by GA. This obtained optimal arrangement of permanent magnets reduced the deflection of the steel plate and could suppress the vibration of the levitated steel plate. When the gap became larger than the optimum gap, the attractive force of the permanent magnets became too small relative to the distance, even though the number of permanent magnets increased. This weakened the effect

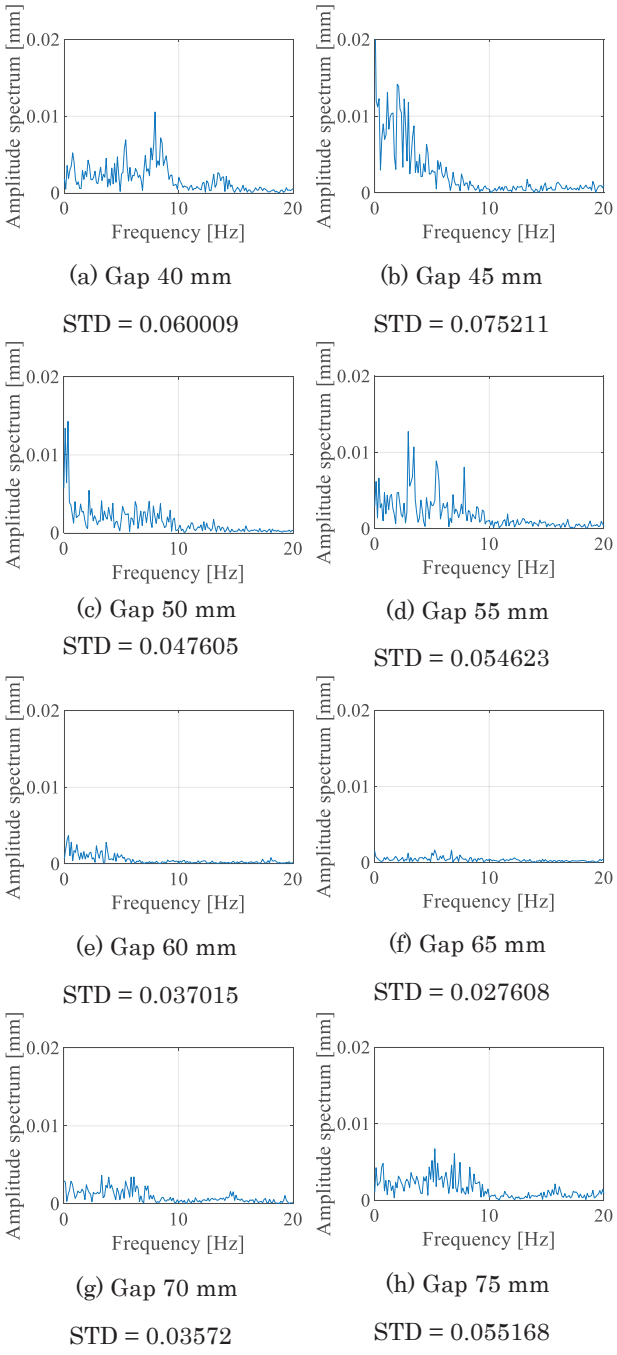

Fig. 8 Spectrum and standard deviation of steel plate at each gap.

of the levitation support, making it impossible to suppress the vibration of the steel plate. The reason for the difference between the optimal gap in the GA search and the optimal gap in the experiment can be attributed to the fact that, when the steel plate is levitated, the gap is larger than the set value owing to the small local deflections in the steel plate. Consequently, the optimal gap of 65 mm, which is 5 mm smaller than the optimal gap of 70 mm in the GA, is considered to be the optimum value in the experiment.

5. Conclusion

In this study, magnetic levitation experiments on steel plates were conducted using an optimal arrangement of permanent magnets when the distance between the permanent magnets and the steel plates was changed, and the vibration waveforms of the steel plates during levitation were compared and discussed. The experimental results confirmed that the levitation performance of the steel plate differed for each gap. The levitation performance of the steel plates differs depending on the gap. When the gap is small and the number of permanent magnets is small, the vibration of the steel plates cannot be suppressed. When the gap is large and the number of permanent magnets that can be installed increases, the vibration of the steel plates can be suppressed. These results show that the proposed method can change the vibration characteristics of a levitated steel plate and improve levitation stability. The present method can be used to optimize the placement of permanent magnets by GA when the material, shape, and thickness of the steel plates are changed. However, in the current phase, only the support is being studied, and it is not yet clear how much disturbance will be applied to the actual conveying process. Therefore, we would like to clarify the vibration state of the steel plate that can be levitated when transported using this arrangement.

References

1) F. Sun and K. Oka: *Trans. Jpn. Soc. Mech. Eng. Ser. C*, **78**, 792 (2012).
2) A. Takabayashi, T. Mizuno, M Takasaki, and Y. Ishino: *Trans. Jpn. Soc. Mech. Eng. Ser. C*, **79**, 801 (2013).
3) M. Sees and S. Torii: *Int. J. Appl. Electromagn. Mech.*, **13**, 1–4 (2001/2002).
4) A. Shiina, S. Kayama, M.N. Hakimi, K. Ogawa, T. Narita, and H. Kato: *T. Magn. Soc. Jpn. (Special Issues).*, **5**, 2 (2021).
5) Y. Oshinoya, S. Kobayashi, and K. Tanno: *Trans. Jpn. Soc. Mech. Eng. Ser. C*, **62**, 600 (1996).
6) Y. Oshinoya and K. Ishibashi: *Trans. Jpn. Soc. Mech. Eng. Ser. C*, **67**, 661 (2001).
7) M. Morishita and T. Azukizawa: *IEEJ Trans. Ind. Appl.*, **108**, 5 (1988).
8) C. Zhao, K. Oka, Feng Sun, A. Harada, J. Jin, and M. Zhang: *IEEE Trans. Ind. Electron.*, **69**, 11 (2022).
9) T. Narita, S. Hasegawa, and Y. Oshinoya: *J. Magn. Soc. Jpn.*, **37**, 2 (2013).
10) T. Suzuki, M. Kida, Y. Oda, T. Narita, H. Kato, and H. Moriyama: *J. Jpn. Soc. Appl. Elec. Mech.*, **26**, 1 (2018).
11) S. Kayama, M.N. Hakimi, A. Shiina, K. Ogawa, A. Endo, T. Narita, and H. Kato: *T. Magn. Soc. Jpn. (Special Issues).*, **6**, 1 (2022).
12) T. Narita, T. Kurihara, and H. Kato: *Mech. Eng. J.*, **3**, 6 (2016).
13) H. Ishii, T. Narita, and H. Kato: *J. Jpn. Soc. Appl. Elec. Mech.*, **24**, 3 (2016).

Received Nov. 09, 2022; Accepted Dec. 20, 2022

J. Magn. Soc. Jpn., **47**, 78-83 (2023) <Paper>

Development of an ANC system with a giant magnetostrictive actuator for ultra-compact electric vehicles: Thrust force characteristics including road noise range

T. Kato*, T. Kitamura**, F. Maehara**, I. Kobayashi**, J. Kuroda**, D. Uchino***, K. Ogawa***, K. Ikeda****, A. Endo*****, H. Kato******, T. Narita******, and M. Furui*

* Department of Mechanical Engineering, Tokyo University of Technology, *1401-1, Katakura, Hachioji-shi, Tokyo 192-0982, Japan*
** Course of Mechanical Engineering, Tokai Univ., *4-1-1 Kitakaname, Hiratsuka-shi, Kanagawa 259-1292, Japan*
*** Course of Science and Technology, Tokai Univ., *4-1-1 Kitakaname, Hiratsuka-shi, Kanagawa 259-1292, Japan*
**** Department of Mechanical Engineering, Hokkaido University of Technology, *7Jo-15-4-1 Maeda, Teine-ku, Sapporo-shi, Hokkaido 006-8585, Japan*
***** Department of Electrical Engineering, Fukuoka Institute of Technology, *3-30-1 Wajirohigashi, Higashi-ku, Fukuoka-shi, Fukuoka 811-1295, Japan*
****** Department of Prime Mover Engineering, Tokai Univ., *4-1-1 Kitakaname, Hiratsuka-shi, Kanagawa 259-1292, Japan*

Ultra-compact electric vehicles (EVs) have been recently sold as next-generation vehicles. However, they are yet to reach a notable phase of expansion and use. Ultra-compact EVs have compact and lightweight bodies. As the outer plate of an ultra-compact EV has low rigidity, the road noise generated by the tires and the wind noise generated from the vehicle's projection shape are transmitted to the interior of the vehicle. Therefore, a new active noise control (ANC) system with a giant magnetostrictive actuator for ultra-compact EVs has been recently proposed. The giant magnetostrictive actuator is required to produce sufficient thrust, with less distortion, and delayed sound waves. In this work, we studied the thrust force characteristics of the giant magnetostrictive material, including in the road noise range. We considered the giant magnetostrictive thrust for output, including in the road noise range, using a finite element model of the giant magnetostrictive actuator by conducting an electromagnetic field analysis. The results showed that the effect of the thrust on the frequency changes depending on the length of the giant magnetostrictive material.

Key words: ultra-compact EV, giant magnetostrictive actuator, finite element model, electromagnetic field analysis, road noise, output characteristics, thrust force

1. Introduction

One- or two-seater ultra-compact electric vehicles (EVs) have been lately sold as next-generation vehicles[1]. This type of vehicle can serve as a new mobility tool, particularly in areas without public transportation or car sharing[2),3)]. However, ultra-compact EVs are yet to reach a notable phase of expansion and use. Ultra-compact EVs are compact and lightweight bodies. Therefore, the rigidity of the outer plate is low. Because of this low rigidity, the road noise generated by the tires and the wind noise generated from the projection shape of the vehicle is transmitted to the cabin[4)]. In a general vehicle, sound-absorbing materials are installed inside the vehicle for soundproofing. Luxury vehicles have an active noise control (ANC) system that controls a sound-generating speaker, which is installed in the cabin[5),6)]. However, it is difficult to install sound-absorbing materials or an ANC system in ultra-compact EVs, given the limited interior space. The demand for ultra-compact EVs is expected to increase in the future, while research and development into noise control systems as noise countermeasures have been insufficient.

Corresponding author: T. Kato (E-mail: katohtr@stf.teuac.jp).

Hence, we have been developing a new ANC system for ultra-compact EVs to improve their interior sound environment. We experimentally clarified the effectiveness of the proposed ANC system in outputting low-frequency sound waves with a high sound quality using wall surface vibration generated by a giant magnetostrictive actuator[7)-13)]. The use of a giant magnetostrictive actuator makes it possible to reduce the impact on the interior space while considering the weight of the ultra-compact EV. Furthermore, we ensured a comfortable interior space by masking the noise present in the cabin by playing the passenger's favorite music[14)-17)]. The ANC system proposed by the authors for ultra-compact EVs uses wall surface vibration generated by a giant magnetostrictive actuator as the source of control sound and masking. In this system, for the output control sound, the giant magnetostrictive actuator must have sufficient thrust, less distortion, and delayed sound waves. In particular, it is essential to maximize the noise reduction value via digital signal processing.

In this study, by performing an electromagnetic field analysis, we analytically investigated the characteristics of the thrust generated by the deformation of a giant magnetostrictive material under

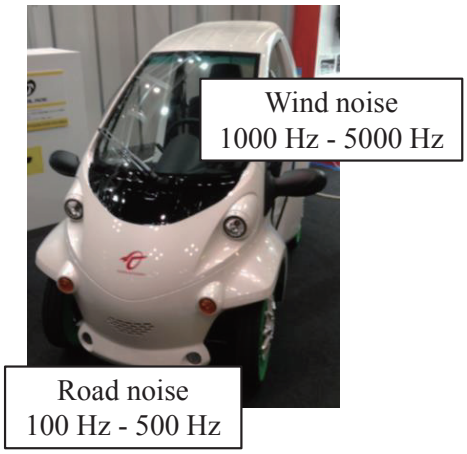

Fig. 1 Image of an ultra-compact electric vehicle, including details on the types of interior noise generated.

Fig. 2 Giant magnetostrictive actuator.

a magnetic field.

We established a finite element model of a giant magnetostrictive actuator with different shapes of the magnetostrictive material. We clarified the difference in the magnetostrictive force when outputting sound at a single frequency ranging from 100 - 500 Hz, which is the frequency band of road noise, depending on the shape of the giant magnetostrictive material.

2. Design of giant magnetostrictive actuator considering output band including road noise range

One of the factors hindering the widespread usage of ultra-compact EVs is the lack of comfort due to noise inside the vehicle, as shown in Fig. 1. Therefore, we have been developing a new ANC system for ultra-compact EVs using a giant magnetostrictive actuator, which is installed on the wall to reduce the impact on the interior space and weight of the vehicle. This system outputs a control sound through the giant magnetostrictive actuator, as shown in Fig. 2 which is installed on the wall inside the vehicle. The value of the sound control effect is most muted at the position of the passenger's ears. In particular, the proposed system targets road noise with frequencies ranging from 100 - 500 Hz[18)-20)], which is difficult to suppress using soundproof materials.

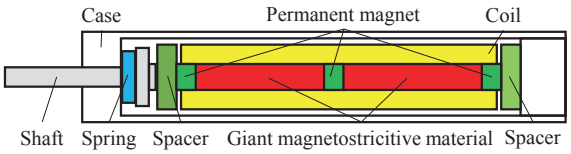

Fig. 3 Structure of a giant magnetostrictive actuator.

Table 1 Details of the giant magnetostrictive actuator.

Components	Material	Electrical resistivity
Permanent magnet	Neodymium sintered (NEOREC27)	-
Shaft/ Spring /Spacer	SUS303	0.7×10^{-6}
Coil	Cu	1.7×10^{-8}
Giant magnetostrictive material	Terfenol-D	6.0×10^{-7}

In this ANC system for ultra-compact EVs, the noise reduction value in the cabin, which comprises the interior noise and passenger's ear position, is affected by the sound field control sound. To increase the noise reduction value using the ANC, the performance of the giant magnetostrictive actuator that can accurately output the signal of the control sound generated by the computer is important in addition to the output of the control sound for noise and phase compensation considering the sound field in the vehicle.

In this study, an electromagnetic field analysis using a finite element model was performed on the magnetostrictive thrust and frequency characteristics as a design of the giant magnetostrictive actuator considering the output band included in the road noise range.

3. Actuator structure and thrust force generated by the giant magnetostrictive material

3.1 Structure of giant magnetostrictive actuator

Fig. 3 shows the structure of the giant magnetostrictive actuator. Fig. 4 shows the dimensions of each part. The giant magnetostrictive actuator comprises a columnar magnetostrictive material, a permanent magnet that applies a bias magnetic field, a solenoid coil, and a spacer. The coil is connected to an AC source, and the magnetic field is generated by the current flowing through the coil. The giant magnetostrictive material is stretched by the magnetic field, and the control sound is outputted by the wall surface generating vibration via the shaft and spring. Table 1 presents the other constituent components and materials of the actuator.

3.2 Generated magnetostrictive thrust force by the current flowing through the coil from the AC source

Fig. 5 shows the model of the giant magnetostrictive actuator cut along the longitudinal direction. The permanent magnet around the giant magnetostrictive material has an N pole on the shaft side and an S pole

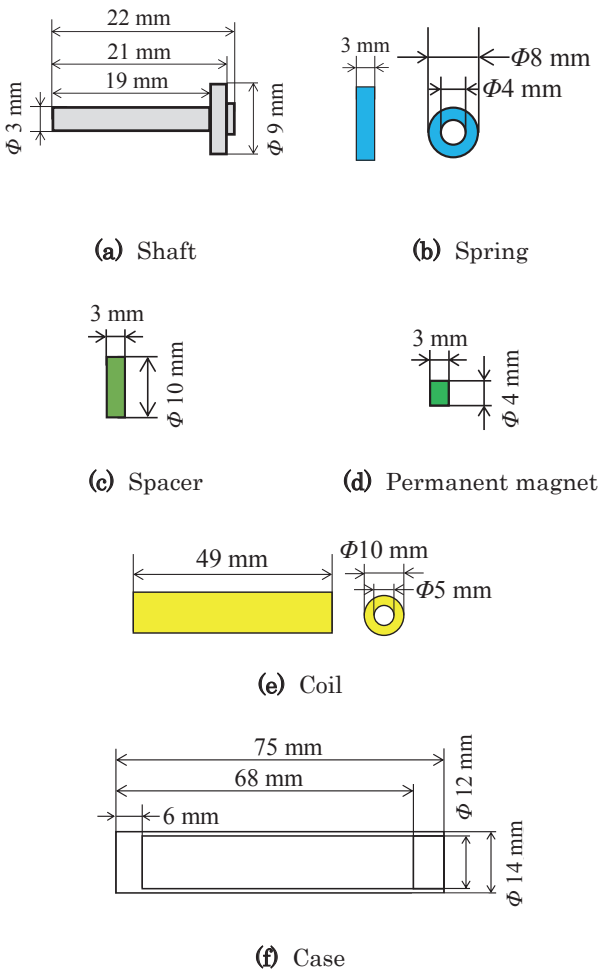

Fig. 4 Dimensions of each part of the giant magnetostrictive actuator.

on the opposite side. In this scenario, the generated giant magnetostrictive thrust on the surface in contact with the shaft will take a positive value. This is because, from Fig. 4, the x-axis direction has an origin on the shaft side, and the left direction is positive. Therefore, the direction in which the shaft is pushed out by the stretched giant magnetostrictive material is positive. Permanent magnets are used as the bias magnets in the magnetostrictive actuator. Therefore, the giant magnetostrictive material generates a constant magnetostrictive thrust force under the effect of the magnetic field applied by the permanent magnet, even though no AC flows through the coil. Subsequently, when the AC flows through the coil, the giant magnetostrictive force generated by the operating giant magnetostrictive material increases or decreases. The thrust force causes the shaft to transmit the vibration to the wall surface. Thus, sound waves are outputted due to vibration.

3.3 Analysis model and material characteristics of the giant magnetostrictive material

In this study, we considered the giant magnetostrictive thrust for the output band included in road noise control

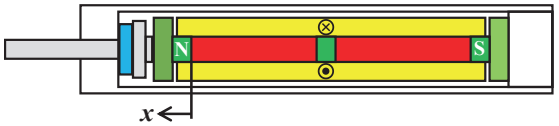

Fig. 5 Model of the giant magnetostrictive actuator cut along the longitudinal direction.

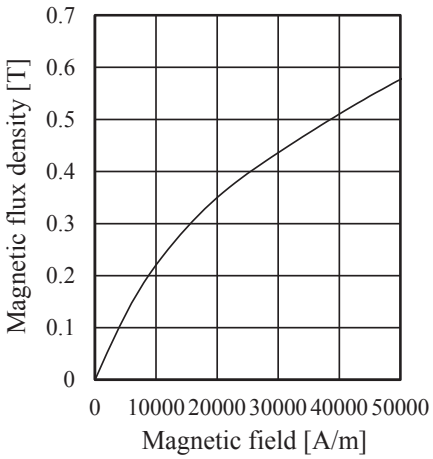

Fig. 6 B–H curve of the magnetostrictive material.

sound using the finite element model of the giant magnetostrictive actuator by conducting an electromagnetic field analysis using JMAG Designer Version 16.0 (JSOL Corporation). The permanent magnet was magnetized in the axial direction of the giant magnetostrictive material. The used coil conductor had a diameter of 0.5 mm, 1000 turns, and an inductance of 3.5 μH.

In this analysis, the characteristics of the giant magnetostrictive material were used as the values of the magnetic field and magnetic flux density according to the research conducted by Sugawara et al.[21], as shown in Fig. 6. The result of the size change under the effect of the external magnetic field applied to the magnetostrictive material was taken according to the research conducted by Mori[22]. The relationship between magnetic flux density and distortion was obtained based on these results, as shown in Fig. 7. The Young's modulus of the giant magnetostrictive material was set to 26.5 GPa and Poisson's ratio value was 0.3.

With these considerations, we conducted a 3D analysis. The number of divided elements was 29653, and the number of nodes was 5570. In the establishment of the electromagnetic field analysis, the shaft and giant magnetostrictive materials were considered to have eddy currents.

4. Analytical study of the magnetostrictive thrust force characteristics due to differences in giant magnetostrictive material shapes

The giant magnetostrictive actuator outputs the displacement due to the axial strain of the material. Therefore, we analytically examined the thrust force characteristics due to the difference in the shapes of the

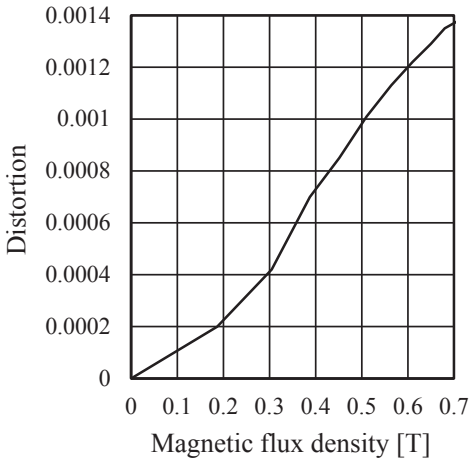

Fig. 7 Relationship between the magnetic flux density and distortion.

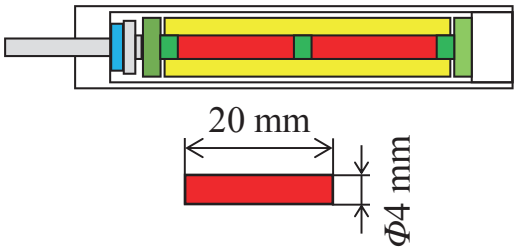

(a) Two Terfenol-D magnetostrictive materials with a length of 20 mm and a diameter of 4 mm (Model A)

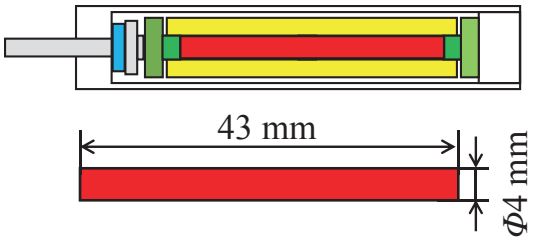

(b) One Terfenol-D magnetostrictive material with a length of 43 mm and a diameter of 4 mm (Model B)

Fig. 8 Finite element models of two giant magnetostrictive actuators.

giant magnetostrictive material.

Fig. 8 shows the finite element models of the two giant magnetostrictive actuators used in this study. Fig. 8(a) shows a giant magnetostrictive actuator in which two Terfenol-D magnetostrictive materials with a length of 20 mm and a diameter of 4 mm are arranged in series. On the other hand, in Fig. 8(b), the giant magnetostrictive material has a length of 43 mm, and two permanent magnets are used. The magnetostrictive thrust force from the giant magnetostrictive material was calculated using Hooke's law by magnetostriction and the magnetic flux density, Poisson's ratio, and Young's modulus.

We analyzed the magnetostrictive force and magnetic flux density with the variation in the AC voltage and the frequency applied to the coil, ranging from 100 to 500 Hz, following the road noise frequency band. In this analysis, the sampling frequency was 20 kHz, and the voltage amplitude was 3 V. When we install the proposed ANC which is using the giant magnetostrictive actuator system for the ultra-compact EV, it is possible to compensate for the output delay of the control sound wave due to the inductance using a current-controlled amplifier. However, when the current control type amplifier increases the impedance of the giant magnetostrictive actuator due to heat generation, the voltage increases to the output commanded current. We considered the actuator may be damaged by high temperatures due to increased voltage. Therefore, we plan to use a voltage-controlled amplifier for the proposed ANC system.

Fig. 9 shows the magnetostrictive thrust force–time history of the finite element model A; Fig. 10 shows the same for the finite element model B. From Fig. 9, the finite element model A has distortion in the thrust force wave shape at 100, 200, and 300 Hz. For this reason, we considered the magnetic field larger than the bias flux flows in the opposite direction to the giant magnetostrictive material by the AC magnetic field of the coil.

However, from Fig. 10, there is no distortion in the thrust force wave shape at frequencies ranging from 200 to 500 Hz in the finite element model B. From both results, we considered that the magnetostrictive thrust of the giant magnetostrictive material is outputted by the displacement due to the axial strain. Therefore, the longer magnetostrictive material can output low-frequency sound waves with high sound quality.

Fig. 11 shows the amplitude values of the magnetostrictive thrust force at each frequency. The results show that model A has a lower thrust than model B at 100 Hz and 200 Hz, whereas model B has a lower thrust at 300 Hz or higher. This is attributed to the fact that the length of the giant magnetostrictive material affects the thrust at each frequency.

5. Conclusions

We developed an ANC system with a giant magnetostrictive actuator for ultra-compact EVs. We considered the giant magnetostrictive thrust for output, including in the road noise range, using the finite element model of the giant magnetostrictive actuator by conducting an electromagnetic field analysis. We clarified the thrust characteristics due to magnetostriction when changing the length of the giant magnetostrictive material, which is one of the elements of the actuator. The results showed that the effect of the thrust on the frequency varies with the length of the giant magnetostrictive material.

In the design of the magnetostrictive actuator, the natural frequency of each element is considered to affect the output characteristics. Therefore, in the future, we will vary the size, weight, shape, and components of the actuator. Moreover, we plan to use a material with higher magnetic permeability.

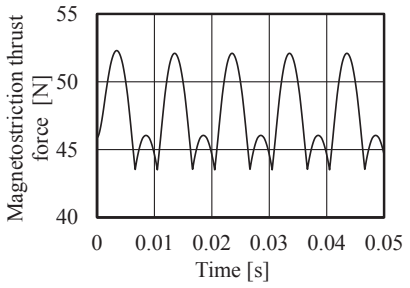

(a) 100 Hz

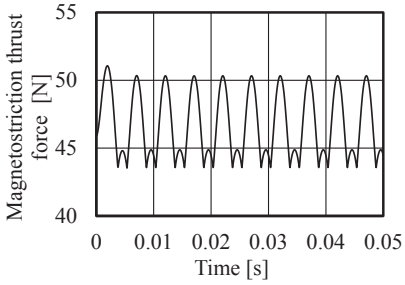

(b) 200 Hz

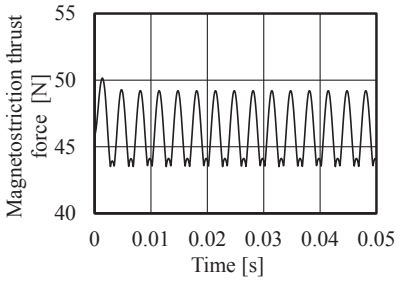

(c) 300 Hz

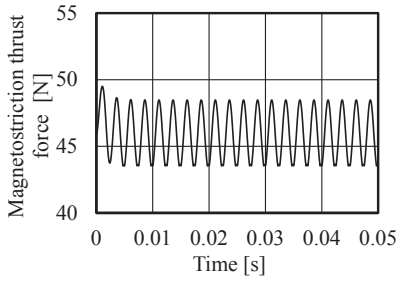

(d) 400 Hz

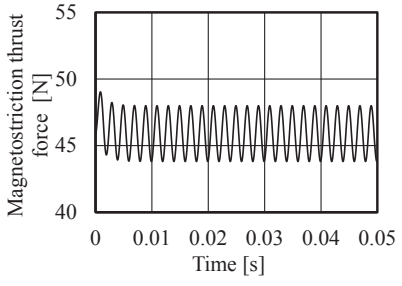

(e) 500 Hz

Fig. 9 Magnetostrictive thrust force–time histories of finite element model A.

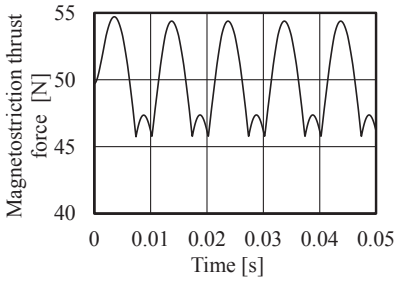

(a) 100 Hz

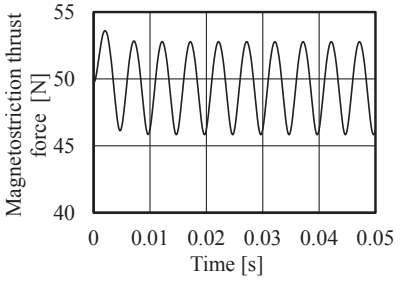

(b) 200 Hz

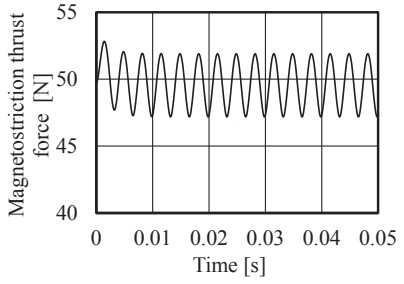

(c) 300 Hz

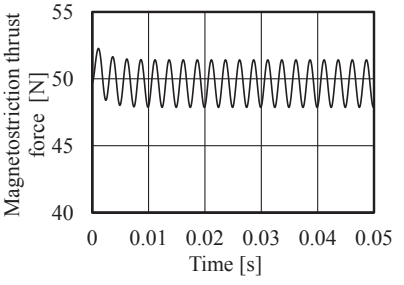

(d) 400 Hz

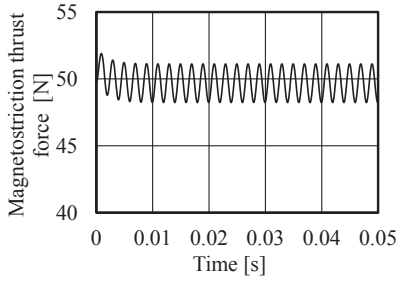

(e) 500 Hz

Fig. 10 Magnetostrictive thrust force–time histories of finite element model B.

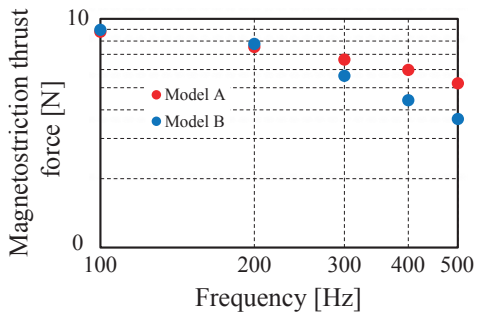

Fig. 11 Amplitude values of the magnetostrictive thrust force at each frequency.

Acknowledgments We acknowledge the support provided by the Japan Keirin Association (JKA), Japan.

References

1) Y. Nishihori and H. Kato: *Trans. JSAE*, **48**, 933 (2017) (in Japanese)
2) Y. Tsuchiya, F. Ito, N, Tagashira, T. Ikeya, K. Baba: *JCPI*, **51**, 46 (2016) (in Japanese)
3) H. Honda: *AJG*, **90**, 590 (2017) (in Japanese).
4) The ministry of Land, Infrastructure, Transport, and Tourism: *Profits on ultra-compact mobility lead to investigation utilizing experiments*, **63**, (2011) (in Japanese).
5) A. Y. Atmojo, Z. Masfuri, M. Sabrina, A. Basuki, Y. Feriadi, Suwarjono, Sugianto: *Journal of Physics Conference Series*, **1951**, (2021).
6) P. N. Samarasinghe, W. Zhang, T. D. Abhayapala: *IEEE Signal Processing Magazine,* **33**, 61, (2016).
7) T. Kato, R. Suzuki, H. Kato, S. Hasegawa, Y. Oshinoya: *Proc., IPEC 2014*, 2972 (2014).
8) R. Suzuki, T. Kato, H. Kato, S. Hasegawa, Y. Oshinoya: *Proc., ICPE 2014*, 774 (2014).
9) T. Kato, H. Nakayama, H. Kato, T. Narita: *Proc., MoViC 2020*, 10079 (2020).
10) T. Kato, R. Suzuki, T. Narita, H. Kato, Y. Yamamoto: *IJAEM*, **52**, 153 (2016).
11) T. Kato, R. Suzuki, R. Miyao, H. Kato, T. Narita: *Actuators*, **7**, 49 (2018).
12) T. Kato, T. Kitamura, F. Maehara, H. Nakayama, K. Ikeda, A. Endo, H. Kato, T. Narita: *Trans. Magn. Special Issue*, **5**, 44 (2021) (in Japanese).
13) T. Kato, T. Kitamura, F. Maehara, H. Nakayama, K. Ikeda, A. Endo, H. Kato, T. Narita: *MSJ*, **46**, 70 (2022).
14) K. Ishizuka, T. Kato, H. Kato, T. Narita, A. Kojima, H. Moriyama: *JAEM*, **25**, 88 (2017) (in Japanese).
15) R. Suzuki, R. Miyao, T. Kato, H. Kato, T. Narita, H. Kikugawa, Y. Matsumura: *Proc. School of Engineering Tokai University, Serise E*, **44**, 22 (2019).
16) T. Kato, H. Nakayama, H. Kato, T. Narita: *Applied Sciences*, **10**, 3412 (2020).
17) T. Kato, T. Kitamura, F. Maehara, D. Uchino, K. Ogawa, K. Ikeda, A. Endo, T. Narita, H. Kato, M. Furui: *Applied Sciences*, **12**, 9425 (2022).
18) N. Yukawa: *Trans. Jpn. Mech. Eng.*, **112**, 426 (2009) (in Japanese).
19) D. Flo, D. Pena, L. Pena, V. A. de Sousa Jr., A. Martins: *Sensors*, **20**, 2471 (2020).
20) Z. Jia, X. Zheng, Q. Zhou, Z. Hao, Y. Qiu: *Sensors*, **20**, 7190, (2020).
21) M. Sugawara and M. Arai: *Trans. Jpn. Soc. Comp. Eng. Sci.*, **7**, 11-080317 (2008) (in Japanese).
22) T. Mori: *J. Robot. Soc. Jpn*, **15**, 334 (1997) (in Japanese).

Received Nov. 11, 2022; Accepted Feb. 17, 2023

Editorial Committee Members・Paper Committee Members

Notice for Photocopying

編集委員・論文委員

複写をされる方へ

Journal of the Magnetics Society of Japan

Vol. 47 No. 3 (通巻第327号) 2023年5月1日発行

Vol. 47 No. 3 Published May 1, 2023
by the Magnetics Society of Japan
Tokyo YWCA building Rm207, 1–8–11 Kanda surugadai, Chiyoda-ku, Tokyo 101–0062
Tel. +81–3–5281–0106 Fax. +81–3–5281–0107

Printed by JP Corporation Co., Ltd.
Sports Plaza building 401, 2–4–3, Shinkamata Ota-ku, Tokyo 144–0054
Advertising agency: Kagaku Gijutsu-sha

発行：(公社)日本磁気学会 101–0062 東京都千代田区神田駿河台 1–8–11 東京YWCA会館 207 号室
製作：ジェイピーシー 144–0054 東京都大田区新蒲田 2–4–3 スポーツプラザビル401 Tel.（03）6715–7915
広告取扱い：科学技術社 111–0052 東京都台東区柳橋 2–10–8 武田ビル 4F Tel.（03）5809–1132